Ge, Y.; Vronka, M.; Veřtát, P.; Karlik, M.; Hannula, S. P.; Heczko, O.

Deformation twinning with different twin-boundary mobility in 2H martensite in Cu–Ni–Al shape memory alloy

Published in:
Acta Materialia

DOI:
10.1016/j.actamat.2021.117598

Published: 01/03/2022

Document Version
Peer-reviewed accepted author manuscript, also known as Final accepted manuscript or Post-print

Deformation twinning with different twin-boundary mobility in 2H martensite in Cu–Ni–Al shape memory alloy

Y. Ge[1,2*], M. Vronka [2], P. Veřtát[2], M. Karlik[3,4], S.-P. Hannula[1] and Oleg Heczko[2]

[1] Aalto University, Department of Chemistry and Materials Science, Espoo, Finland

[2] FZU - Institute of Physics of the Czech Academy of Sciences, Prague, Czech Republic

[3] Czech Technical University in Prague, Department of Materials, Prague, Czech Republic

[4] Charles University, Department of Physics of Materials, Prague, Czech Republic

Abstract

Three possible twinning modes, Type I, Type II, and compound, as well as corresponding twin boundaries in 2H martensite of $Cu_{69.4}Ni_{3.4}Al_{27.2}$ single crystal, were studied by X-ray diffraction (XRD) and high-resolution transmission electron microscopy (HRTEM). The results are discussed with regard to the sharply different twinning stress or twin-boundary mobility. In self-accommodated martensite, all three modes not only coexist but are crystallographically coupled. The compound twin boundary is a coherent coplanar mirror plane with the smallest twinning shear. The Type II twin boundary is also a coherent strain-free interface. The high index rational approximation of Type II twin boundary was determined by trace analysis with the help of stereographic projection. The approximation is in good agreement with irrational indices calculated from elastic continuum. The Type I boundary is the most complex interface associated with high stress and high density of stacking faults inside the twin bands. Using HRTEM, two different stressed boundaries of Type I were confirmed. The intrinsic twinning mode in Cu-Ni-Al alloy is the compound twinning. In compression, the Type II twinning is the major deformation twinning mode. During deformation the Type I twins are eliminated, leaving Type II twinning bands with compound twins. The observed differences between the atomic structure of different twin boundaries can contribute significantly to the sharp differences in twinning stress.

Keywords: shape memory alloys, deformation twinning, twinning stress, single crystal, HRTEM

* Corresponding authors' e-mail: yanling.ge@vtt.fi; present address: VTT Technical Research Centre of Finland P.O. Box 1000, FI-02044 VTT, Finland

1. Introduction

The Cu–Ni–Al is an often-studied prototype of shape memory alloy (SMA) [1], owing to its relatively simple crystal structure, availability of single crystals, and transformation temperature close to room temperature. The single crystal of Cu-Ni-Al exhibits a large transformation strain, repeatability, and resistance against transformation fracture, with good compatibility between transforming phases [2,3]. The single crystals also exhibit relatively low twinning stress or a high mobility of twin boundaries in the martensitic phase [4].

High mobility of twin boundaries in shape memory alloys is often noted but the reason behind this has not been studied thoroughly [4-6]. The research in this field has gained a new momentum by the discovery of magnetic shape memory effect [7], or magnetically-induced reorientation of martensitic (MIR) variants [8], resulting in a giant magnetic field-induced deformation up to 12 % in Ni-Mn-Ga single crystals [9]. In order to manipulate the martensitic microstructure by magnetic field [10], the extremely high mobility of twin boundaries is crucial. Nevertheless, the reason for this high mobility is still unknown and detailed studies of twin boundaries are needed. Unfortunately, the ferromagnetic character of the alloy, high mobility of the twin boundary in a magnetic field, and relative brittleness of modulated Ni–Mn–Ga martensite made the studies difficult or even impossible [11]. In recent work [4, 11], we have shown that a particular Cu–Ni–Al single crystal having mobile twin boundaries [12] can be considered as a non-magnetic analogue to Ni–Mn–Ga magnetic shape memory alloy. We can expect that detailed studies of deformation twinning and involved twin boundaries in Cu–Ni–Al help to clarify the reason for the high mobility of twin boundaries in general, and particularly for extreme mobility in Ni-Mn-Ga.

Cu–Ni–Al shape memory alloys with $D0_3$ ordered parent β austenitic phase transforms into modulated 2H or 18R martensite or into a mixture of both, depending on the alloy composition, temperature, magnitude, and the sense of applied stress and orientation of the crystals [12-15]. Asymmetry between tension and compression stress-induced transformation was observed. A modulated 2H structure is preferred during compression while a 18R structure is preferred during tension [13]. In spontaneous transformation without any external stress, both structures occurred due to local internal stress on phase interface [16].

Here, we will focus on the 2H martensite, as these twinned microstructures exhibit sharply different twinning stress for different twin boundaries and fairly low twinning stress in compound twins comparable to twinning stress in Ni–Mn–Ga [2,15]. The term 2H originated from the consideration of the structure as hexagonal with unit cell exhibiting 2H modulation. The structure is characterized by an AB´ stacking sequence [17]. This is a hcp-based superstructure because the alternative (110) planes shift their position by about 1/12 of the nearest atomic distance along [$\bar{1}$10] direction from the ideally close-packed position seen in Fig.1. The 2H stacking thus means two layers per H(exagonal) unit cell in Ramsdell's notation.

Most of the previous works describe the 2H martensite of Cu–Ni–Al using the orthorhombic system with a *Pnmm* (#59) space group, having two basic axes originating from the face-diagonal of the cubic austenite lattice, and the third axis along the edge of the cubic unit cell. For an easier description of the transformation from austenite to martensite, we use a monoclinic lattice which enables the preservation of the same notation of crystal planes and directions in the austenite and in the martensite. The details are given in Ref. [11]. The lattice parameters for the monoclinic description of the 2H martensite are $a = b = 6.089$ Å, $c = 5.368$ Å, and $\gamma = 92.07°$ [12]. With this interpretation and using an adaptive concept [18], the 2H martensite can be viewed as composed from two-layered nanotwins. This kind of alternating sequence of nanotwins is analogous with modulated martensite in Ni–Mn–Ga [19,20]. The shuffling of (110) planes then cause additional superstructure reflection in the diffraction pattern.

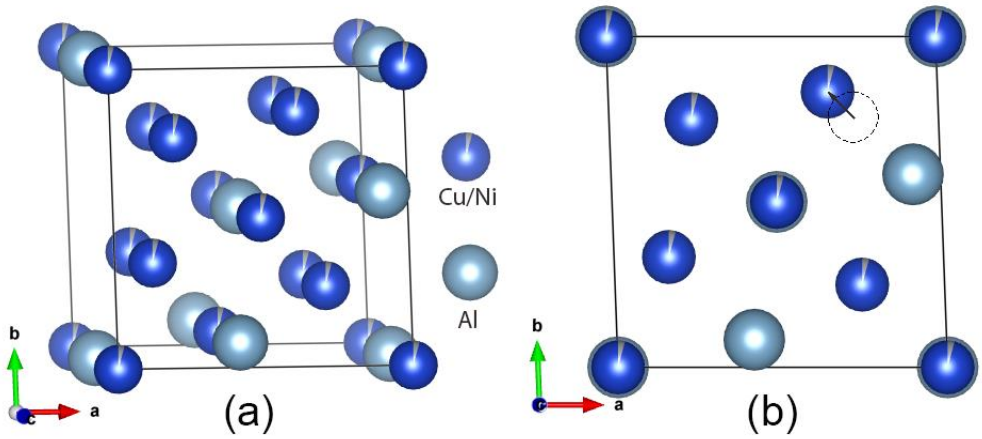

Fig. 1. (a) Unit cell of $Cu_{69.4}Ni_{3.4}Al_{27.2}$ with basis along the cubic coordinate system; (b) the projection of unit cell along [001] direction. The shuffling direction of atoms of alternation (110) plane is indicated by an arrow.

The 2H martensite has three possible deformation twinning modes - compound, Type I, and Type II twinning - in agreement with the general theory of monoclinic twinning [14,21,22]. Type I twinning is characterized by the rational twinning plane but irrational twinning shear vector (two twin crystals are related by the mirror symmetry with respect to the twinning plane). Contrarily, Type II twinning is characterized by the irrational twinning plane but rational twinning shear vector (two twin crystals are related by rotation of 180° around twinning shear direction) [23], making Type I and Type II twinning a conjugate or reciprocal mode to each other [24]. The third mode of twinning, the compound twins, are two variants of martensite bordering such that both the twinning plane and the twinning shear vectors are rational [21,25].

The main findings of electron microscopy studies [22,23,26-28] focusing on the investigation of the twinning boundaries in Cu–Ni–Al can be summarized as follows. According to [22,29], both martensitic structures, i.e. 2H and 18R martensite, coexist together when Al content is around 13 wt% [1]. A large number of stacking faults were found in the 18R structure [29]. In the 2H phase, all three types of twins expected from the theory were observed [23,27,29]. It was found that the width of Type I twin bands was much smaller, only about 0.2 μm, compared to Type II bands, which were several μm wide [23]. Furthermore, Type I twins were often found inside Type II twin bands, or they were observed mainly near edges of the specimens [23]. The Type I deformation twining has been discovered in this alloy during tensile test [30] with twinning stress over 20 MPa, however this twining mode has not been observed in compression test. In large strain compression Type II twinning is a prevalent deformation mode with twinning stress of approximately 20 MPa or even less [4]. However, the Type II twinning stress sharply increased with decreasing dimensions following scaling power law with an exponent approximately n = - 2/3 [28]. For very small nanopillars, the projected twinning stress was so high that the nanopillars were deformed by plastic deformation instead of twinning [28].

The compound twin exhibited about 10 times lower twinning stress, 1-2 MPa, compared to Type II twinning [30] [4]. Observed twinning stress lower than 1 MPa [4] is comparable to twinning stress in Ni-Mn-Ga [31] even for compound twinning as demonstrated recently. The Cu–Ni–Al alloy bears other similarities to the Ni–Mn–Ga system. Both alloys, the twinning stress show a large difference between Type I, Type II, and compound twinning modes [32,33]. It is a well-established concept that in the Cu–Ni–Al alloy no distinction can be made between the mechanism of the deformation twinning and transformation twinning [26]. This

is also true for a Ni–Mn–Ga alloy, where the twins formed during martensitic transformation are identical with those formed by deformation in martensitic state, and the thermally-induced twins can be deformed during detwinning process right after phase transformation [34].

Despite of vast sum of accumulated knowledge in Cu–Ni–Al shape memory alloys, there is no detailed and comparative study of deformation twinning by high resolution transmission electron microscopy (HRTEM) completed at the atomic scale with possible atomic configurations at the boundaries. Furthermore, none of the studies links the mobility of the twin boundary to its morphology. The purpose of this paper is to present and discuss a detailed and comparative transmission electron microscope (TEM) and X-ray diffraction (XRD) study of all deformation twinning structures in 2H Cu–Ni–Al martensite in attempt to enlighten the origin of the high mobility of twin boundaries in general.

2. Experiment

The single crystal ingot of $Cu_{69.4}Ni_{3.4}Al_{27.2}$ (at%) alloy was grown by the Bridgman technique and was annealed at 950 °C for 1 h in an argon atmosphere and quenched in a mixture of ice and water. The resulting structure at room temperature was 2H martensite, confirmed by the X-ray diffraction. The composition of single crystals was characterized by Flame Atomic Absorption Spectrometry and Energy Dispersive X-ray Spectroscopy.

For TEM studies, three 1 mm thick plates with self-accommodated martensitic structures were spark cut with surface plane normals close to [100], [110] and [111] crystal lattice orientations in the austenitic state. The slices were then reduced by grinding to 100 μm and then punched into 3 mm diameter discs that were thinned to the final thickness in the central part by double jet electropolishing at -20° in a solution of 30% HNO_3 in methyl alcohol. For X-ray diffraction studies, we used a cuboid specimen with dimensions of 7 mm x 4.7 mm x 4 mm. The largest side was polished in the austenite state and had (100) orientation. The other sides were inclined 27° from (010) and (001). The specimen was deformed over the second largest side to generate twinning and to obtain twin bands visible at the largest side similar to the reference [12]. The X-ray diffraction measurements were taken from this side.

The conventional TEM and HRTEM observations were carried out by FEI Tecnai F20 field emission gun transmission electron microscope operated at 200 kV with a double tilt

specimen holder. All schemes of the crystal structures and twin morphologies were prepared with VESTA 3 software [35].

X-ray diffraction (XRD) experiments were carried out on PANalytical X'Pert PRO diffractometer in Bragg-Brentano geometry with point focus. Cu anode was used as an X-ray source. The sample was attached to the ATC-3 texture cradle which served as a goniometer. The orientation of the samples was determined in the austenitic state based on pole figure measurements.

3. Results

Three deformation twinning mode in the 2H martensite are described in the monoclinic lattice notation as {101) Type I, <101] Type II and {100) compound twinning. In the investigated single crystals under compression, the deformation mode is compound twinning at very low twining stress, i.e., less than 2 MPa, followed by Type II twinning with the stress about 20 MPa [12]. Fig. 2a shows an optical micrograph of the Type II twin variants resulting from an incomplete detwinning process. The deformation twinning system was first studied by X-Ray diffraction (XRD). XRD measurements confirmed the lattice parameters in $Cu_{69.4}Ni_{3.4}Al_{27.2}$ as a = 6.089 Å, b = 6.089 Å, c = 5.368 Å, and γ = 92.07 °. Importantly, no traces of 18R phase were found in the XRD measurement.

The X-ray pole figure of {404} reflections is shown in Fig. 2b. The four strongest peaks indicate the orientation of two variants with a twinning relation. However, the twinning mode cannot be unambiguously determined by the {404} reflections without orientation information of other poles. Additionally, four small satellite reflections were observed around each of these {404} reflections. They were determined by repeatedly measuring each of the satellite reflections along the 2Θ axis as $53\bar{1}$, 531, 351 and $35\bar{1}$ reflections. The plane spacing of {351} is 1.009Å which is very close to the plane spacing of {404}, 1.006Å, i.e. a 0.5 degree difference in 2Θ. Courtesy of the used X-ray optics, the reflections of {531} are all visible in the {404} pole figure. This is very useful for the determination of the twin relationship because their position related to the {404} pole are sensitive to rotation or mirror symmetry. Thus, the Type II twinning relationship between four strong {404} poles can be determined unambiguously by satellite reflections of {351}. The position of these reflections confirmed that all {404} peaks originated from two compound twins in agreement with optical observation (Fig. 2a). In conclusion, the {404} pole figure in Fig. 2b consists of four variants

- Type II twinning pairs and two compound twins apparently within the Type II twins as shown below.

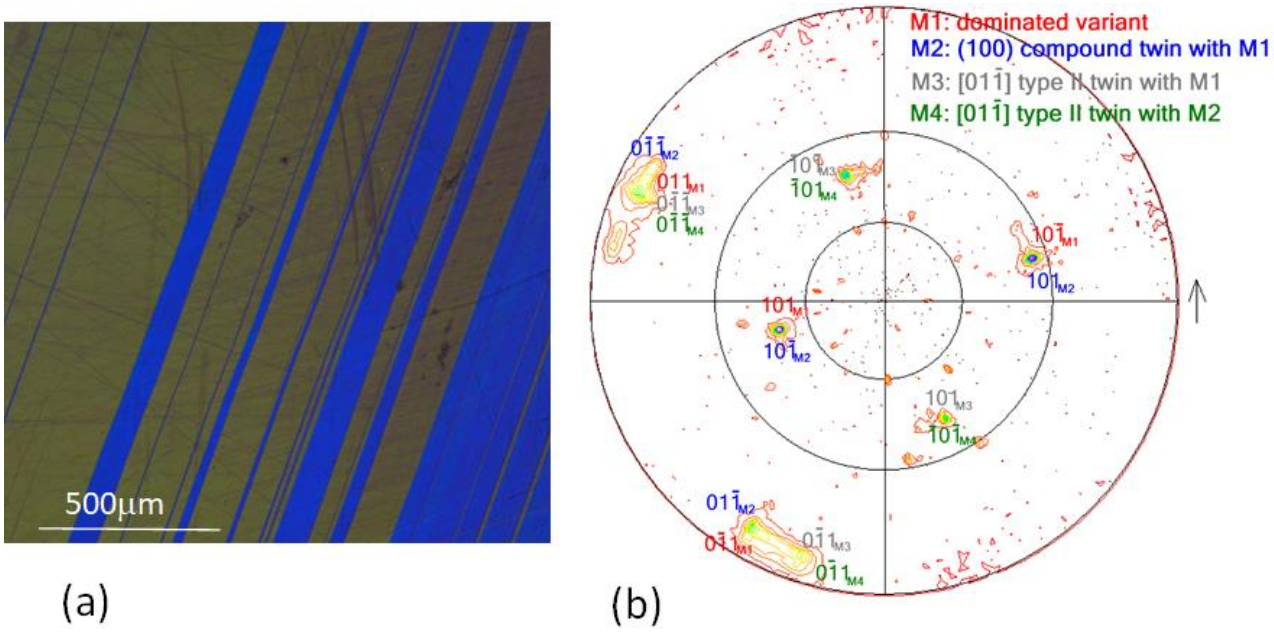

Fig. 2. (a) Optical image of Type II twin variants in polarized light and (b) {404} pole figure recorded from the same area as in (a).

The XRD reciprocal space mapping (RSM) confirmed the coexistence of the compound twins and Type II twins. Fig. 3a was measured along [001] direction and mainly consists of compound twins of M1 and M2 in Fig. 2b. Fig. 3b was measured along [010] direction of Type II twin variants M1 and M3 in Fig. 2b, and it revealed both compound twins and Type II twins. The other two streaks around each reflection which are parallel and perpendicular to the goniometer axis, respectively are caused by the X-ray optics. The (100) compound twin and [01$\bar{1}$] Type II twin are consistent with the {404} pole figure (Fig. 2b). The compound twins are also clearly visible in Fig.3b, in which RSM maximizes Type II twin intensity. Since the optical image in Fig. 2a shows only contrast from Type II twins, the large amount of compound twins revealed by the XRD pole figure and by RSM must be located inside of Type II twins. This suggests that compound twins are the lowest level in the hierarchical martensitic structure.

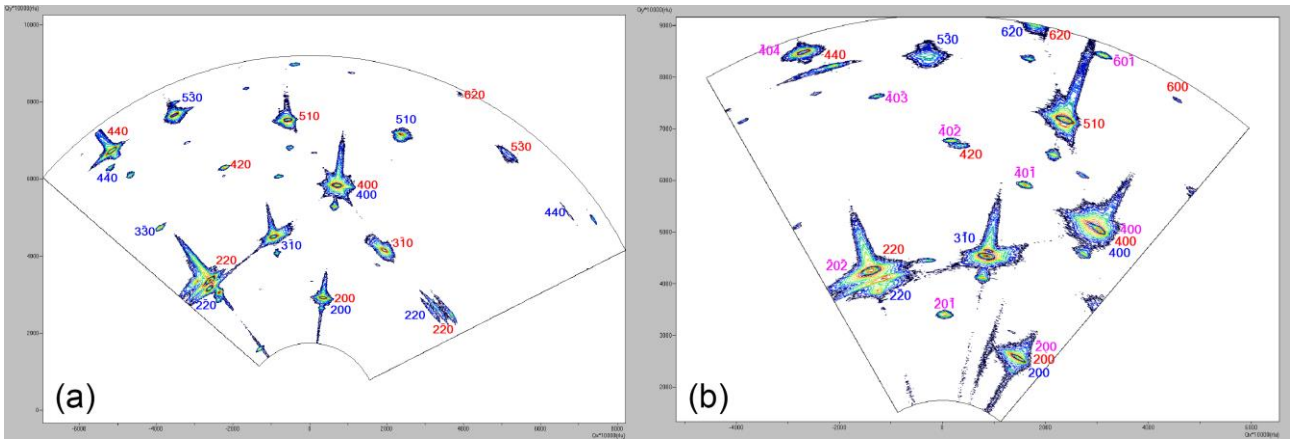

Fig 3. (a) RSM along [001] direction with compound twins M1 and M2. (b) RSM along [010] direction with both compound twin and Type II twin, M1, M2 and M3. (The red indices belong to dominating variants, blue ones are compound twin variants and gray ones are [01$\bar{1}$] type II twin variants as in Fig 2b).

To understand the formation of twinning structures, we prepared three TEM foils with different orientations, i.e., <100>, <111>, and <110> direction normal to the foil surface. To observe all three twinning modes and the possible relationship between them, all foils were prepared from the self-accommodated martensite. It is known that the crystallography of the twins is the same for thermally-induced and stress-induced twins in shape memory alloy [1] and the detwinning mechanism is the same as the twinning mechanism in deformation twins [11]. Thus, the self-accommodated martensitic structure is a key to understand detwinning process during training and obtaining a single variant condition. Moreover, it can explain significant mechanical stabilization of martensite [16,36].

To evaluate the homogeneity of the self-accommodated structure, we compared the lattice parameters obtained from XRD with those measured with selected area electron diffraction (SAED) patterns and from HRTEM images. Fig. 4a shows an HRTEM image in [001] projection which reveals ABAB stacking and basal plane stacking faults. The value of lattice parameters *a* and *b* and angle γ was obtained using fast Fourier transformation (FFT) of the HRTEM image. Figs. 4b and 4c show two typical SAED patterns corresponding to two zone axes (ZA) of [001] and [010], respectively. From these two orientations, the value of *a*, *b*, *c* and γ angle can be directly determined. Due to double reflections, the 2$\bar{2}$0 reflection is almost as strong as the 220 reflection. This results in weak reflections related to plane shuffling, such as {310}, apparent in Fig 4c.

The typical configuration of a self-accommodated martensite structure with all three possible types of twins is shown in Fig. 4d, taken from the foil with <111> orientation using high angle annular dark field (HAADF) detector in scanning TEM mode (STEM). Area B contains a set of perfect Type I twins. The areas A and C are in the Type II twinning relationship to major twins of area B. The boundary between area C and D is a compound twin boundary. It can be concluded that the Type I twin boundary is straight, as expected, and the Type II seems to be straight too in this scale as well. In contrast, the compound twin boundary can have apparently any shape, suggesting that it is the most flexible. This is similar to compound twins observed in Ni-Mn-Ga [37]. In general, for all observed foils, the common features are the following: the Type I twinning is the finest with the smallest dimension, compound twins have dimensions in the range from several nanometers to a few micrometers, and Type II twins have dimensions at least several hundreds of nanometers.

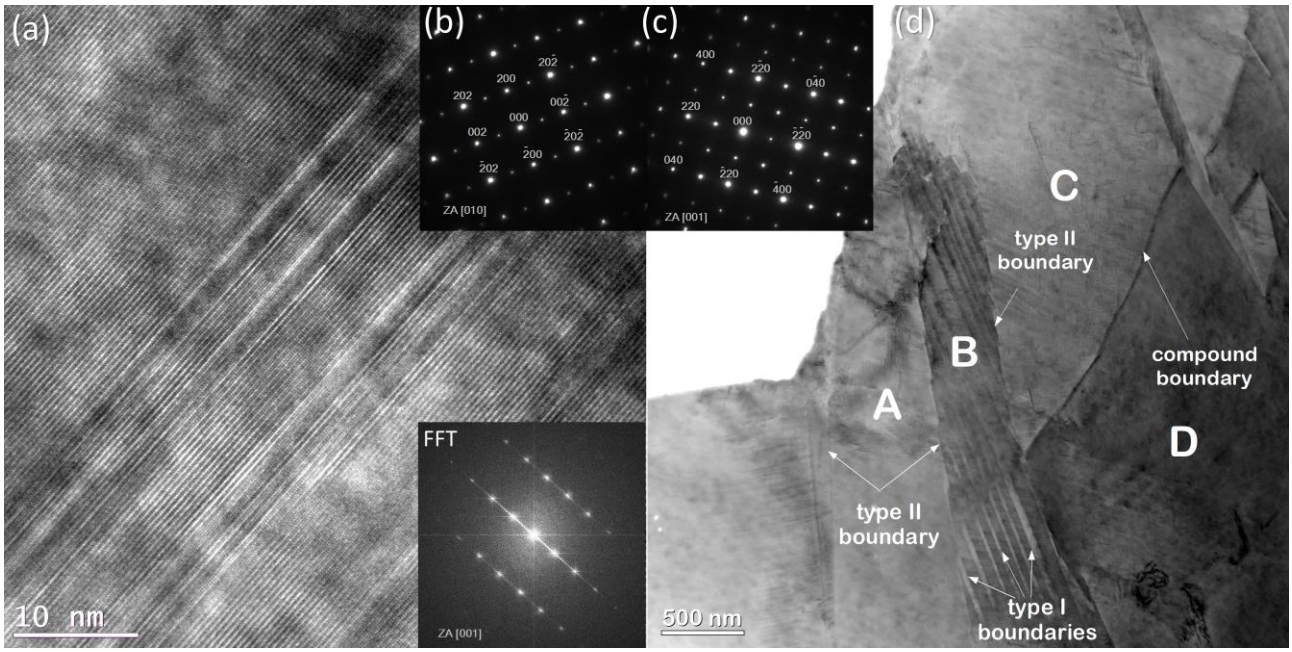

Fig. 4. (a) HRTEM image of the 2H martensite and the corresponding FFT in the inset; SAED patterns from (b) ZA [010] and (c) ZA [001]; and (d) STEM HAADF image with inverse contrast showing the coexistence of three types of twinning variants.

The area with Type I twin pairs always have a step-like boundary with its relatively large neighbor twins, such as the boundary between areas B and A and the boundary between areas B and C in Fig 4d. The kink point, or the step, in the Type II boundary is caused by the compound twin relationship of minor twins in area B with area A. A detail of such boundary with one step is presented in Fig. 5a. Bright field (BF) TEM micrograph shows Type I twinning variants along $[\bar{1}1\bar{1}]$ direction for major twin set B1, which is parallel to $[1\bar{1}1]$

direction of minor twin set B2. A corresponding SAED pattern is in Fig. 5b. The BF image clearly reveals a high density of the basal plane faults inside Type I twin pairs. The electron diffraction pattern confirms Type I twinning relationship, i.e. reflection related to (011) twinning. The Type I twin boundaries appear in the BF image as sharp and straight coplanar interfaces. The variant A has a Type II twinning relationship with the major twins B1, i.e. 180° rotation about $[01\bar{1}]$, as it can be seen from the SAED pattern in Fig. 5c. The orientation between variant A and minor twin variant B2 of Type I pairs was found to be very close to compound twins with respect to (100) plane with a 2.8° deviation. In summary, the step-like boundary consists of mainly Type II boundary, with a short step of a compound twin boundary depending on the width of the minor variant of Type I twin pairs. By trace analysis from different zone axes using stereo projection method, Type II twin boundary was determined to be close to $(7,\overline{22},\overline{22})$ plane, which is in good agreement with the calculated Type II plane $(22,\overline{69},\overline{69})$ [12].

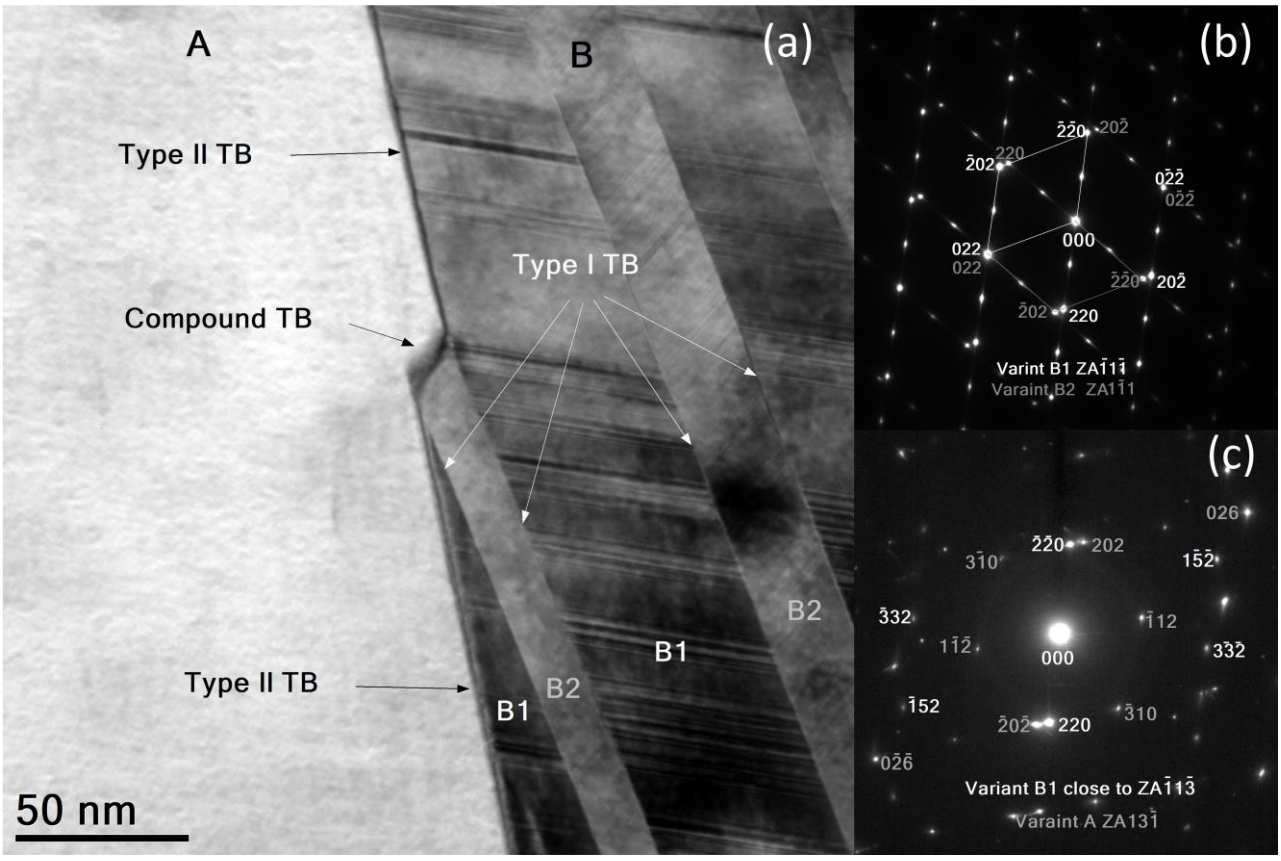

Fig. 5. (a) A TEM BF micrograph shows three correlated types of twin variants: Type I, Type II and compound twin. (b) SAED pattern of Type I twins B1 and B2. (c) SAED pattern of Type II twins A and B1.

Even though the Type I twin boundaries in a BF image (Fig. 6a) appear sharp and straight, at the atomic scale of an HRTEM image (Fig. 6b) these boundaries are more complex than a straight planar interface. First, the twin boundary is a perfect planar interface only if the interface is free of defects, i.e. there are no stacking faults in either side of the twin interface. In the presence of stacking faults, the twin boundary is shifted into the adjacent twin plane by one, or even several atomic layers. It can be seen in the right bottom area of Fig. 6b, that the crossing of faults from two sides is forming a very thick and complex boundary. As Fig. 6a shows, the density of stacking faults is high and thus the majority of Type I boundary is associated with a strain field. This prevents the obtaining of the diffraction contrast (bright field) at high magnification.

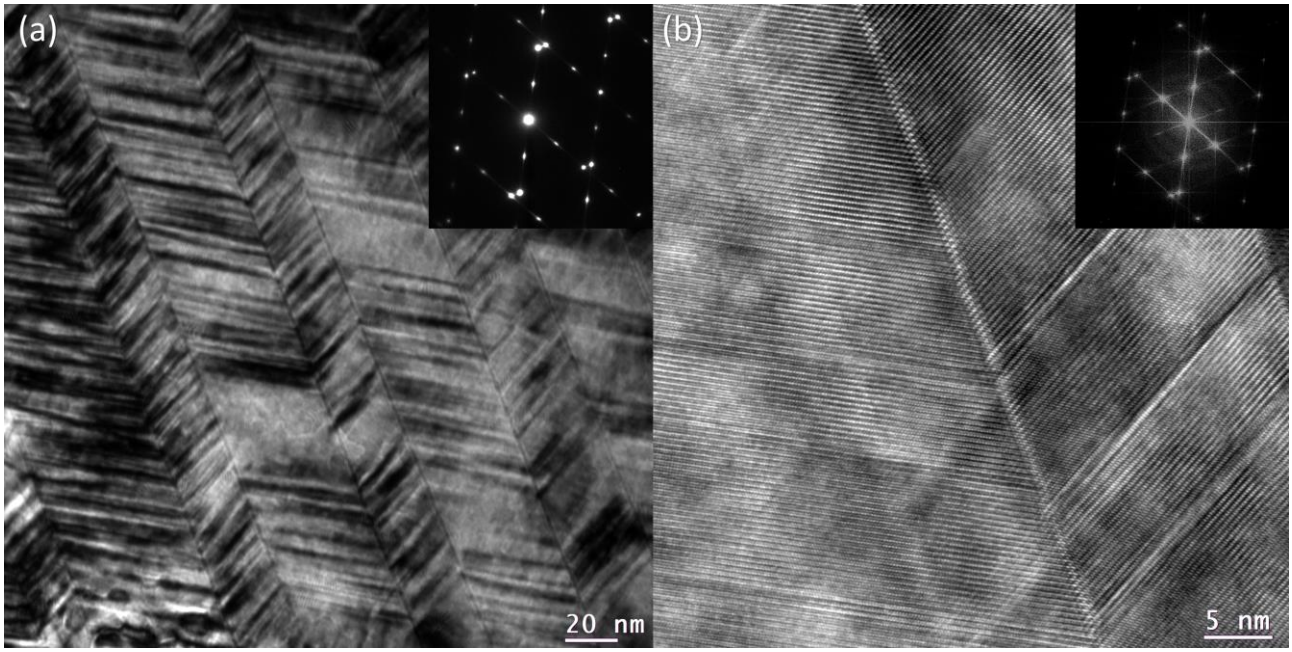

Fig. 6 Type I twins with high density of stacking faults. (a) BF image and corresponding SAED pattern obtained from the boundary area. (b) HRTEM image aligned in the same zone axis as BF image; the FFT is in the inset.

To clarify the atomic configuration of Type I twinning boundary, almost fault-free interfaces were searched. HRTEM images of such interfaces are showed in Fig 7. Although the (011) twin boundary is still a planar interface in both micrographs, the interface in Fig. 7a is relaxed, providing a mirror plane for both sides of the twins, while the interface in Fig. 7c is somewhat more distorted by local stress. The interplanar spacing at the interfaces was measured by a profile function in DigitalMicrograph. The (022) plane (parallel to twin boundary) spacing was measured from 4 planes which just cross the interface and is compared with the rest of the (022) plane spacing inside green the line framed area in Fig. 7a and Fig. 7b, respectively.

According to XRD measurement of the bulk, the (022) plane distance is 2.013 Å. In Fig. 7a and 7b, the near-interface plane distance is 2.16 Å and the average plane distance is 2.00 Å determined by FFT of the whole imaged area. However, in Fig. 7c and 7d, the near interface plane distance is about 1.96Å and the average plane distance is 1.98 Å. It is clear that the planes next to the interface in Fig. 7a are stretched and the planes next to the interface in Fig. 7c are compressed.

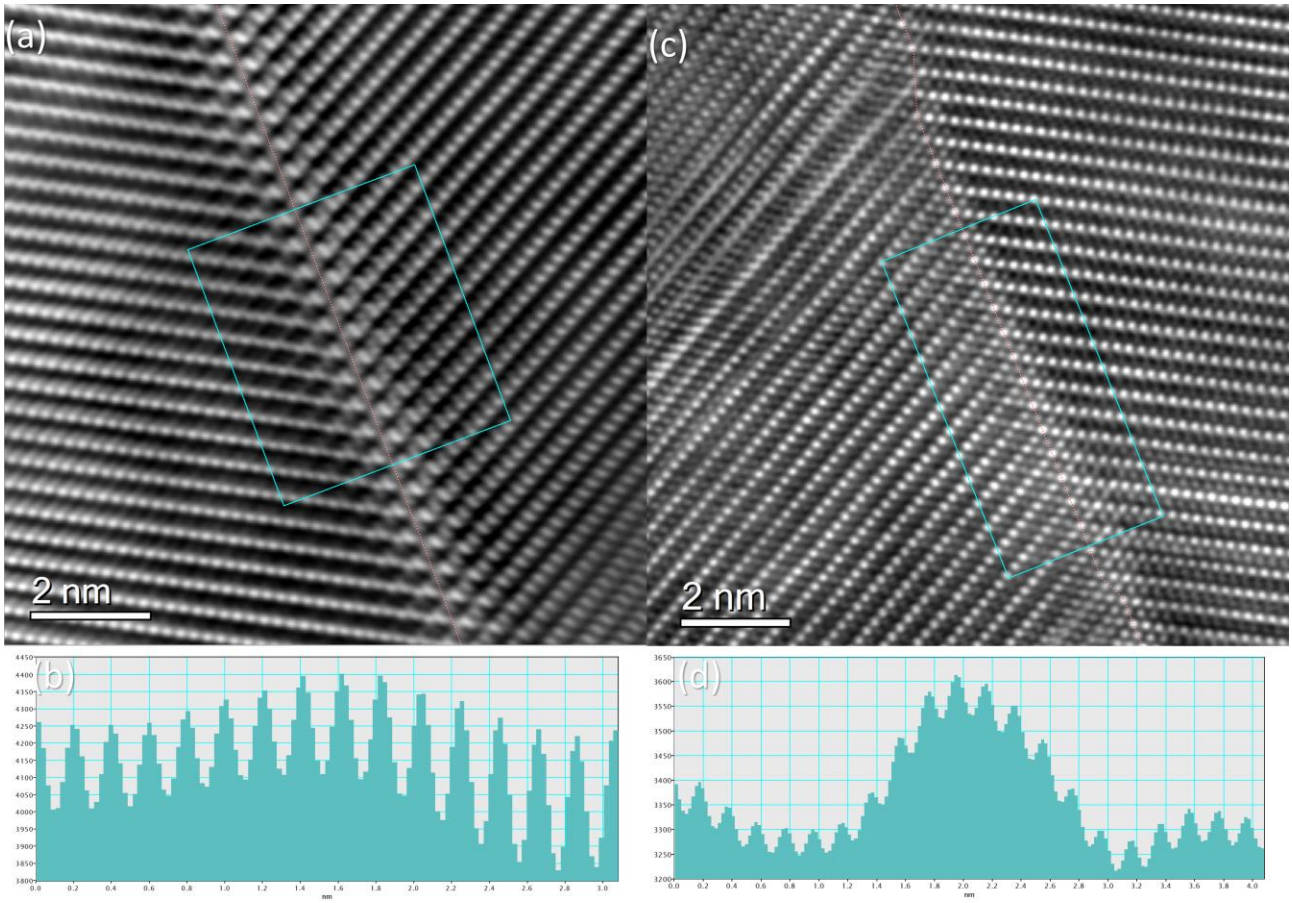

Fig. 7. HRTEM image (FFT filtered) of Type I twinning boundary (a) and (c) and the profile of (022) plane distance near the twin boundary (b) and (d). The twin boundary is marked with red dashed line for eye guidance.

The set of parallel Type II twins, which are common in the deformed bulk sample, as seen in Fig.2, are shown in Fig. 8a. The SAED patterns from two sets of twins confirmed Type II twinning relationship with respect to the [01$\bar{1}$] axis. Due to the view axis along [110] the Type II twin boundary is inclined to the zone axis and not in edge-on position. The twin boundary determined in this orientation is around ($1\bar{4}4$). In Fig. 8b, the single twin variant is [011] Type II twin with respect to the matrix on both its sides. The right side of the matrix is in (100) compound twin relation with the matrix on the left side of the micrograph. A detail of this

Type II boundary is revealed by HRTEM in Fig. 8c. The Type II variant T at the right side of the boundary is aligned along ZA [$31\bar{1}$] and shows perfect lattice fringes. The matrix at the left side of the boundary is close to ZA [$\overline{311}$], about 3 degrees off the zone axis, and thus due to this misorientation, the lattice fringes contrast is weak and blurred. The Type II boundary is determined along ($\overline{299}$) plane. Even though the Type II twin boundary is not in the exact edge-on position, but is inclined to ZA [$31\bar{1}$] about 57.7 °, the HRTEM micrograph still shows clear lattice fringes in inclined twin boundary area (between dashed red lines). The HRTEM of the twin boundary area indicate that the Type II boundary is more or less straight without any visible deformation inside the boundary area. The red dashed lines, marking the intersection of the twin boundary with the foil surface at the top and bottom, are parallel to each other and follow the trace of the twin boundary in Fig. 8b quite well. This suggests that the Type II twin boundary is a coherent coplanar boundary.

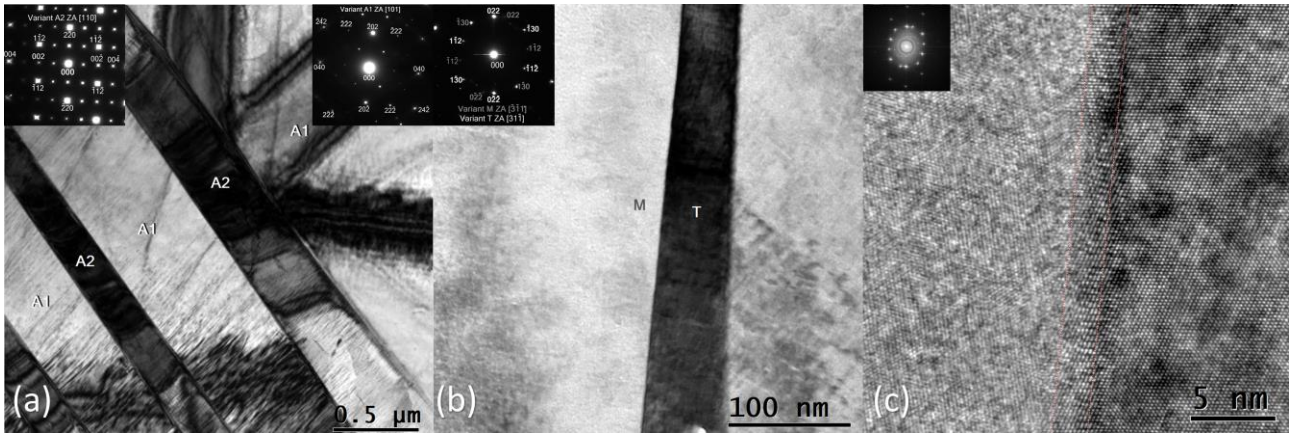

Fig 8. The Type II twins BF and HRTEM. (a) The set of parallel Type II twins and corresponding SAED patterns from the first twin band and upper-right part of the matrix. (b) single plate of [011] Type II twin variant and SAED pattern from left twin boundary area along ZA [$31\bar{1}$]. (c) HRTEM image of the left twin boundary in (b) and its FFT, the dashed lines are traces of the inclined twin boundary with the surfaces of the foil.

The compound twin boundary is the most common and versatile twin boundary in this alloy. These boundaries were found to be either straight or wavy. Fig. 9a shows a set of (100) compound twins along [001] zone axis. The HRTEM image of this type of boundary is seen in Fig. 9b, which shows that the boundary is a perfect coherent coplanar interface without any sign of strain at the boundary. Furthermore, the atomic structure on the boundary is not even affected by stacking faults ending at the interface, as observed in Ni-Mn-Ga [34].

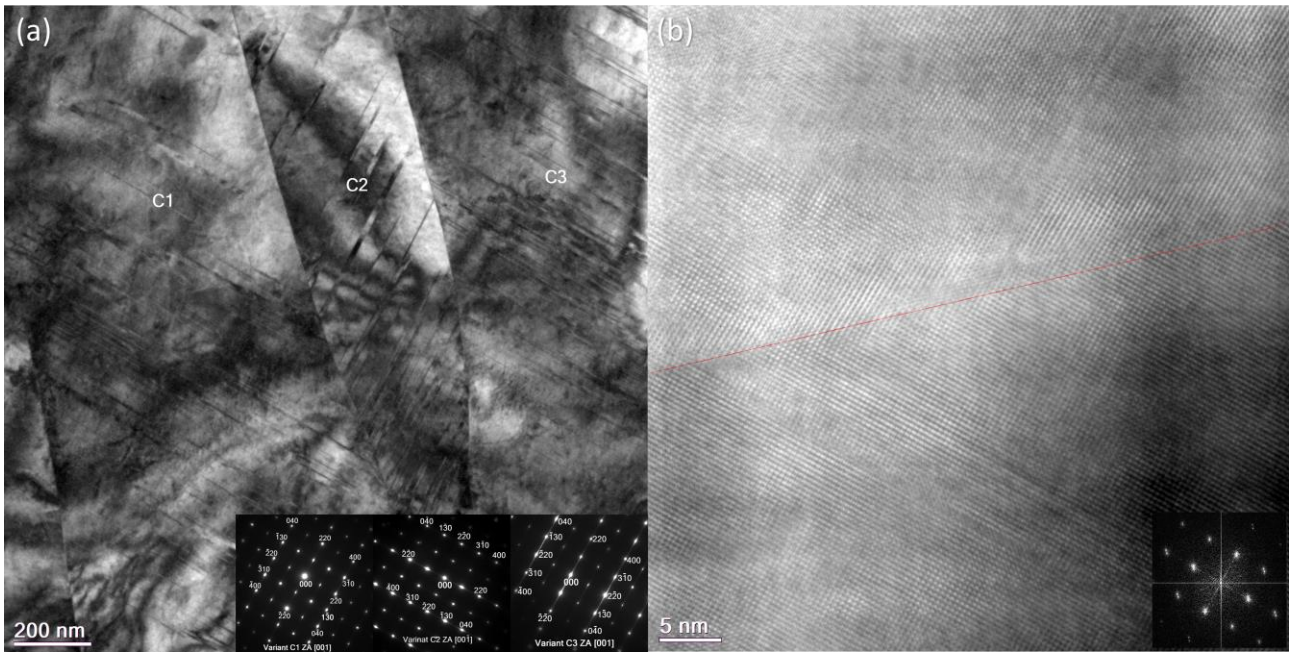

Fig. 9. (a) Compound twins: (a) Bright field TEM micrograph close to [001] zone axis, the inset shows corresponding diffraction patterns in areas C1, C2 and C3, (b) HRTEM of a compound twin boundary (marked by a dashed red line) and its FFT.

In a detail survey of the prepared foils, we found a small amount of 18R martensite in some areas. It may be present in the original bulk but not detected by XRD or it may be induced during foil preparation. TEM micrographs of the phase are shown in Fig. 10a and in high resolution in Fig.10b. Compared to the 2H martensite, the 18R phase contains much more basal plane stacking faults. In a small fault free-area, HRTEM confirmed a perfect $(2\bar{1})$ stacking sequence (Fig. 10b). The average lattice of 18R determined from SAED patterns and FFTs of HRTEM was monoclinic: a = 6.28Å, b = 5.96Å, c = 5.37Å, γ = 92.2°.

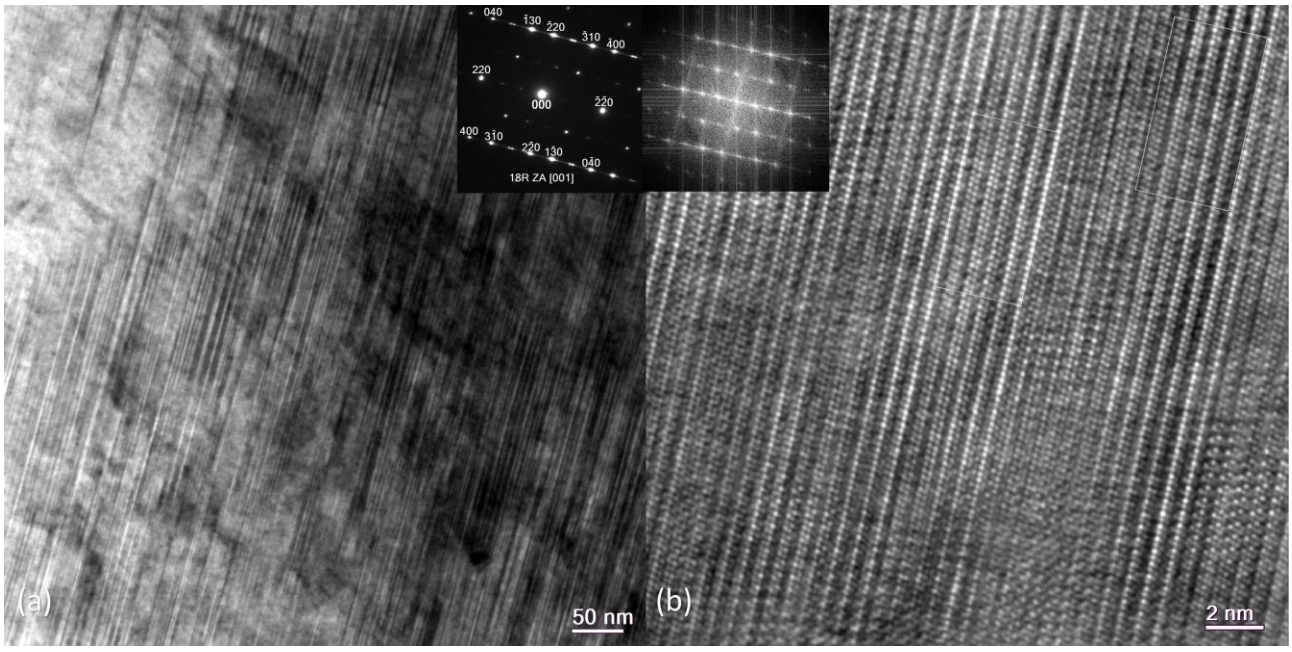

Fig 10. (a) 18R BF image and (b) HRTEM showing $(2\bar{1})$ stacking order with its FFT in inset. Two perfect $(2\bar{1})$ area are marked by rectangular frames.

4. Discussion

The lattice parameters of thin foils determined from HRTEM FFTs and SAED patterns were well in line with the parameters measured by XRD on bulk material in 2H martensite. In general, all three theoretically possible twinning modes were found in this alloy. The Type I twinning mode is a reflection related to {101) K_1 plane, and the Type II twinning mode is a rotation of 180° about <101] η_1 direction. By using simple shear mechanism together with the restriction of crystallography of twinning relationship and lattice symmetry, the approximate rational twinning elements can be obtained from the stereographic projection for both twinning modes. This estimation is meaningful and valuable because the experimental analysis can only provide the rational Miller indices closest to the twinning plane, not the mathematically determined irrational indexation. Here we provide some examples.

Using HRTEM, we determined that the twinning elements for (011) Type I twinning are: K_1 = (011); η_1=[$1\bar{4}\bar{4}$]; K_2= (8,$\bar{2}\bar{5}$,25); η_2=[011], with the shear plane P= $(81\bar{1})$. The twinning shear s can be calculated from rotation angle θ of η_2 direction during twinning as s =2tan(θ/2) = 0.257. The twinning elements of $[01\bar{1}]$ Type II twinning are K_1 = $(8,\bar{2}\bar{5},\bar{2}\bar{5})$; η_1=$[01\bar{1}]$; K_2= $(01\bar{1})$; η_2=$[1\bar{4}\bar{4}]$ and shear plane is P = (811).. The twinning shear calculated for Type II

twinning is the same as for Type I twinning because the rotation angle of η_2 is the same, i.e., s = 0.257. The irrational twinning elements calculated from elastic continuum are (0.2231, 0.6893, 0.6893) when using XRD lattice parameters from bulk. For comparison, if it is normalized to have only one irrational number then it becomes (0.32366, 1, 1), while our closed rational estimation is (0.32, 1, 1). Thus, they are about 0.13° apart. The maximum deviation angle in all experimentally determined Type II planes was 6.29° from the calculated irrational plane. The three measured Type II twin boundaries $(7,\overline{22},\overline{22})$ in Fig 5, and $(\overline{1}44)$ and $(\overline{2},\overline{9},9)$ in Fig 8, deviate from calculated irrational planes about 0.2°, 2.72°, and 3.69°, respectively.

Based on our high-resolution studies of twins, we suggest different models of the twin boundaries and discuss their validity. The possible atomic configurations of (011) Type I twin plane is drawn in Fig. 11, assuming simple shear twinning mechanism. Due to 2H stacking structure, the Type I twinning plane is corrugated. The calculated width of a corrugated twin plane is δ_{011} = 0.33613 Å. The twinning shear direction indicated by the letter s with a gray arrow is along the vertical direction and parallel to the twin boundary. A simple shear can bring the unit cell to a twin position, but atoms inside the unit cell still need further shuffling to be in the final twinning symmetry position [38]. The movement of atoms inside the unit cell can be imagined as firstly shuffling back to a balance position, then going through twinning shear, and then shuffling to a new twinning position [39]. While this mental picture can help understanding the path of atoms, the atoms physically move to the final position via the shortest path. Moreover, the atoms at the interface could go through a different path than the atoms next to the interface.

Fig. 11 illustrates four possible atomic configurations for Type I twinning interface appearing due to the different coincidence sites of atoms at the boundary. In each configuration, the picture on the left shows the state before shuffling of atoms at the interface, and the right one shows the final state after shuffling. The interface is constructed to be in a balanced position for both sides of atomic configurations while keeping a planar boundary.

In Fig. 11a, the interface has half of the atoms coincident and half of the atoms shifted to the balanced position. The shuffling distance is equal to the corrugated plane width δ_{011}, but the atoms´ direction of moving is perpendicular to both twin boundary and shear direction. The atomic distance next to the interface is decreased in this case, thus the interface is under compressive stress. However, the resulting interface is a straight coherent mirror

plane. In Fig. 11b, again half of the atoms at the interface are coincident and half of the atoms need shuffle displacement into a balanced position but the atomic distance next to interface is increased in this case, resulting in the interface being under tensile stress. The shuffling distance is again equal to δ_{011} and perpendicular to the interface. This will also result in a flat coherent mirror plane.

Fig. 11c shows a different situation when all atoms in the interface have to shuffle $\delta_{011}/2$ perpendicular to the interface. Then the interface is also kept flat and coherent and mirror symmetry is preserved.

The final configuration in Fig. 11d is similar to Fig. 11c, but half of the atoms at the interface need to shuffle by $\delta_{011}/2$ along the interface. Here, the resulting interface is not a mirror plane although it is coherent, but it is not flat. Its corrugation fits two sides of the crystals which are crystallographically in the Type I twinning relationship, but atoms inside the unit cell are not in a twin position, so this atomic configuration does not correspond to a true twin.

Our experimental observation confirmed the existence of a twin boundary with decreased and increased lattice spacings near the interface as suggested in Fig. 11 a, b. The interface in Fig. 11c should be a favorable one because it has the smallest shuffling with a flat coplanar interface. This was observed in a similar 2H martensite in Cu-Zn-Al alloy [40]. However, this kind of boundary was not found in our HRTEM studies, most likely due to a high density of faults in Type I twins. The configuration in Fig. 11d, which also has a minimum shuffling and the same direction of shuffling as for twinning shear, is theoretically favorable. Despite this, the corrugated twinning interface has never been found in an experiment. From our observation it can be concluded that the Type I boundary is a mixture of atomic configurations shown in Fig. 11 a and b, and strongly affected by the high density of stacking faults.

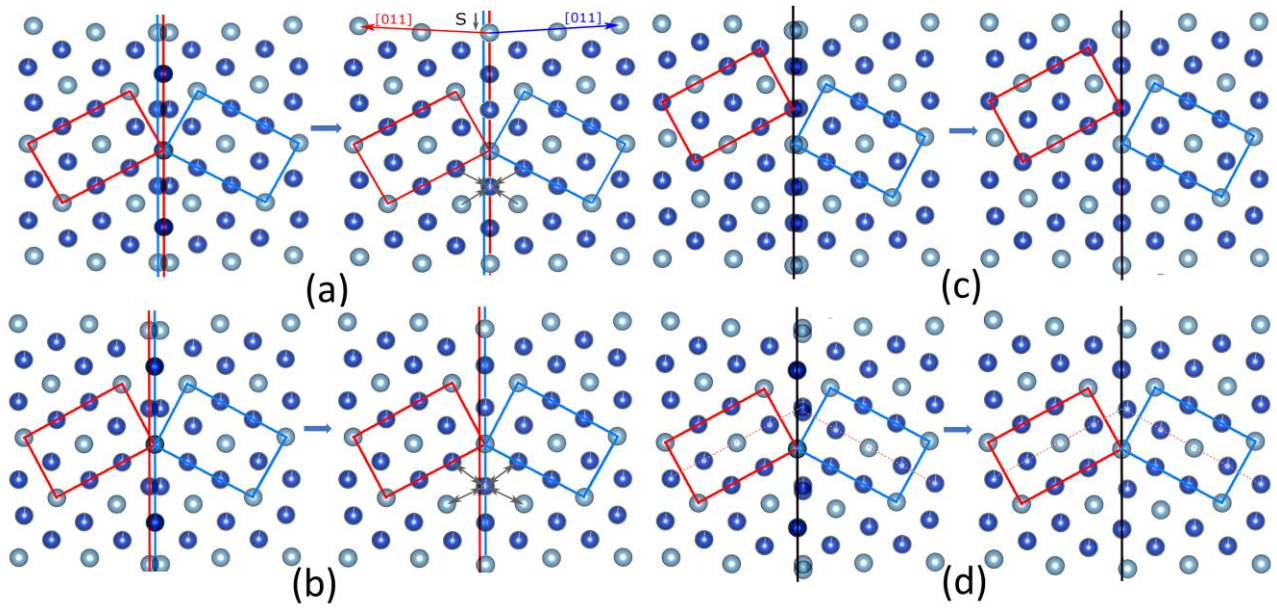

Fig. 11. The four possible atomic models of the Type I twin interface (011) viewed along [1$\bar{1}$1] direction. Left images represent interfaces before shuffling of the atoms and the right ones resulting interfaces after shuffling. In the illustration each atom with its second nearest atoms are in same level of lattice plane. Four cases are listed: (a) the interatomic distance is decreased on both sides of the interface marked with a single arrow line. (b) The interatomic distance is increased marked by a double arrow line. (c) Almost no change of interatomic distance at the interface with small atom shuffling perpendicular to the interface. (d) No changes of the interatomic distances occur at the interface resulting in corrugated pattern.

Fig. 12a illustrates the atomic configuration of a Type II twin boundary ($\bar{8}$,25,25) viewed along the rotation axis [0$\bar{1}$1]. Because the twin boundary is parallel to the rotation axis, it looks like the rotated crystal is identical to the matrix. There is no shuffling of atoms perpendicular to the twin boundary for Type II twinning, resulting in a simple coherent planar interface compared to the complicated stressed Type I twin boundary. The shuffling within the twin boundary is shown in Fig. 12b, where the atoms from the matrix and the twin are both placed on the twin boundary and the overlap of atoms is an indication of shuffling. It is clear that shuffling is needed only on a minority of Cu sites. The shuffling needed is about 0.2618Å and about 1/12 of atoms has to shuffle to a balanced position.

Although the trace analysis indicated that the Type II boundaries are very close to ($\bar{8}$,25,25), still a few different Miller indices were observed. Errors can arise from inherent inaccuracy of tilt angle in TEM and bending of thin foil, from the local equilibrium condition, such as

residual strain, affecting the Type II boundary's identity. In this case it is suggested that the irrational indices of Type II twin boundary have to beak down to rational facets on an atomic scale which would reduce the boundary energy [24,41,42]. This possibility was drawn also in Fig. 12a with a dashed line. The Type II interface ($\bar{8}$,25,25) may be decomposed into two facets periodically spaced, (400) and (022), with lengths of 2.013 Å and 9.1335 Å, respectively. Two facets are parallel to compound twin plane and Type I twin plane. If the length along (022) plane change and/or with non-periodic spacing, then the slope of trace of twin boundary will change, resulting in different boundary index. In this way the stepped boundary is able to adapt with local residual strain as suggested in NiTi alloy [41]. A thermodynamic model suggested that the coherently faceted Type II boundary is nucleated by kink pair on the crystal surface with a very low energy comparable to thermal activation energy down to 11 K [43]. Though the edge on position of Type II boundary was not observed in the present study, the Type II interface in Fig. 8c shows no evidence of such steps at the twin boundary. Additionally, steps at the interface increase the interface area and thus the energy of the twin boundary. Moreover, the continuous Type II interface without steps was also observed in Ni-Mn-Ga [44] indicate it is energy favorable. Topological model of straight Type II boundary suggests that it can host glissile disconnection arrays which result in high mobility and fast interface migration [45]. Thus the investigation about edge-on position HRTEM image at boundary should be carried out to study further the suggested versatile morphology of Type II twin boundary.

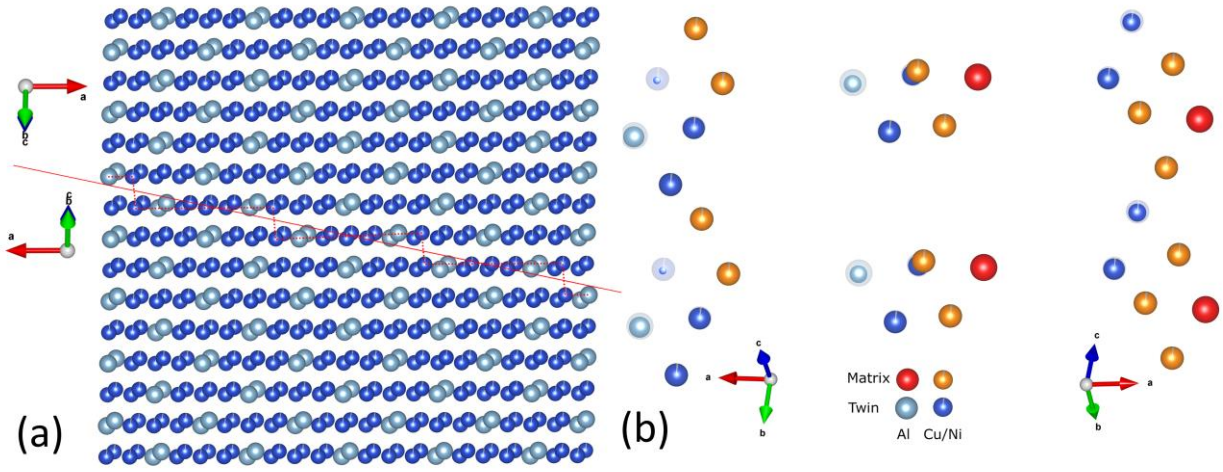

Fig12. (a) The atomic configuration of the Type II twin interface ($\bar{8}$,25,25) viewed along the [0$\bar{1}$1] direction. The horizontal row of atoms indicates the Type I boundary (011) which is perpendicular to the paper. (b) Atoms at the boundary are viewed along the normal of the twin boundary ($\bar{8}$,25,25), with the twin boundary inserted as a transparency layer.

Our observations and suggested atomic model of Type II boundary, which involves minimal shuffling at the interface with a small boundary area, allows a reasonable conclusion that Type II boundary is a straight coplanar interface.

The third type of twinning, the compound twins, can be formed by a simple shear similarly to the Type I twin boundaries. The twinning shear can be calculated from γ lattice parameter as $s = 2\tan(\gamma\text{-}90) = 0.074$. This twinning shear is very small and is consistent with low twinning stress for twinning/detwinning of this type of twin. Due to the shuffling of the 2H structure, the simple shear cannot bring all atoms to the final twinning position, requiring the atoms inside the unit cell to shuffle again. The movement of the atoms inside the unit cell can be disassembled into the following three steps: first, all atoms in the unit cell go through simple shear, then shuffled atoms go back to the balanced position and atoms at the alternative new (110) plane shuffle again. Again, this disassembly of movements is just to facilitate understanding, because in reality atoms take the shortest path to the final position. However, the twin interface {100) is corrugated due to 2H structure. It is energetically unfavorable to have corrugated twinning interface as this causes stress in one side of the twin interface. Thus, the atoms at the interface shuffle back to balanced position to keep a straight and balanced twin interface.

Two possible atomic configurations considering different coincident atoms at the interface are proposed in Fig. 13. Both configurations result in a straight coherent planar interface, however in Fig. 13a the interatomic distances next to the interface are increased while in Fig. 13b the interatomic distances next to the interface are decreased. The shuffling distance is equal with the width of corrugation of (010) plane $\delta_{010} = 0.0835$ Å. Since this distance is very small the shuffling in compound twinning can be ignored. The smallest twinning shear and also minimum atom shuffling at the boundary in compound twin can be related to the lowest twinning stress from all available twinning.

The XRD pole figure measurement indicates that the compound twinning is intrinsic twinning mode, a build-in feature in this alloy. This is confirmed by a deformation experiment. The maximum theoretical shape strain from this twinning mode occurs in a diagonal direction <110> and the value is limited by the difference of magnitude of lattice vectors [110] and $[\bar{1}10]$. The maximum shape strain along [110] direction is calculated as (8.77-8.45)/8.77 = 0.0365, i.e. 3.65%. In contrast, the maximum experimentally observed strain is only about 2% [11] which indicates that the compound twins are always presented in the sample.

Apparently, the compound twins cannot be detwinned completely due to their low twinning stress and smallest twinning shear which require the least atom shuffling.

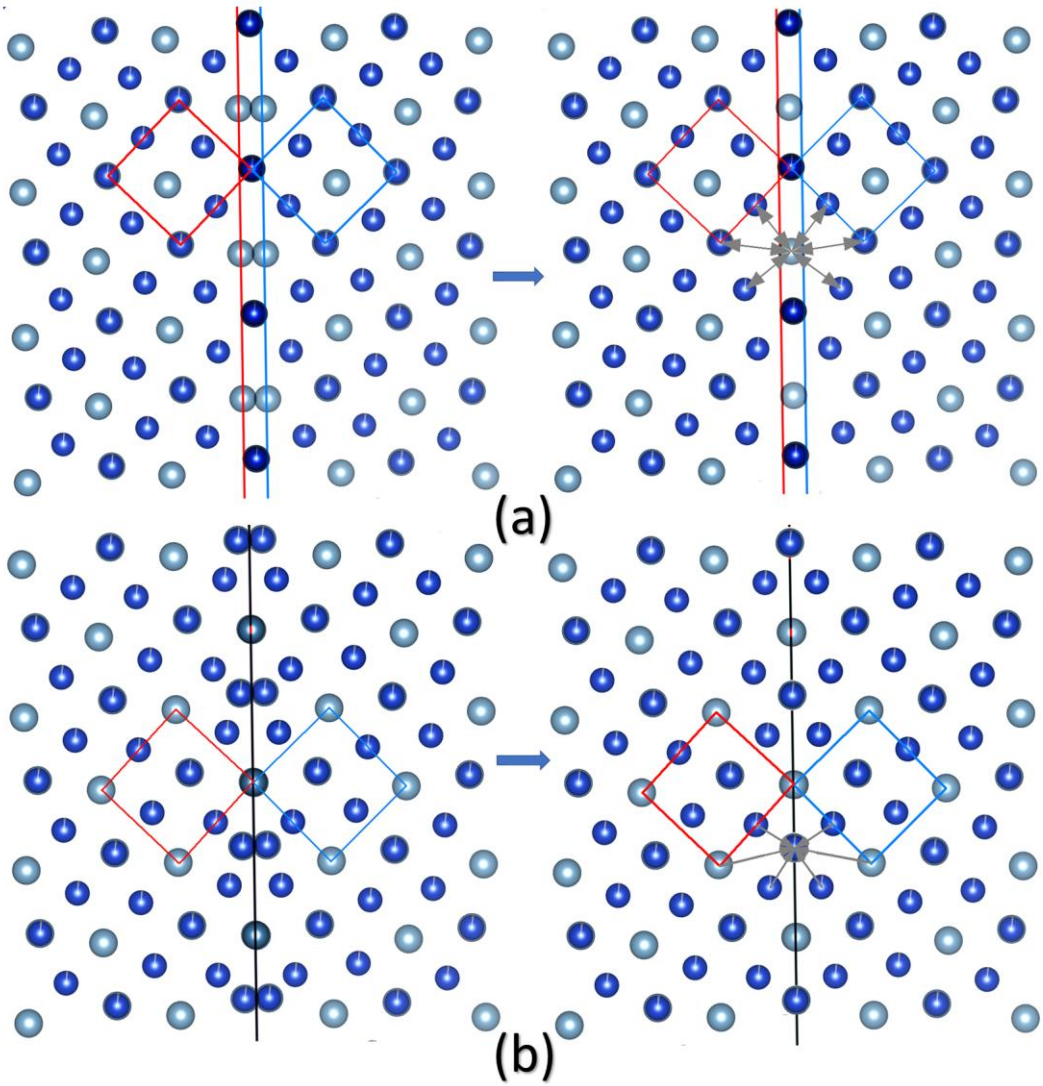

Fig. 13. Two possible atomic configurations of compound twin interface. The view direction is along [001] and compound twin boundary is (010).

In summary, while the twin shear is the same for Type I and Type II twinning, the compound twin has the smallest twin shear. The Type I twin boundary is the most complex boundary. Two atomic configurations need half of the atoms at the interface to shuffle about 0.336 Å perpendicular to the interface which has been confirmed by experimental observation. Two other configurations need half of the atoms at the interface to shuffle about 0.168Å to the balance positions. However, these theoretically-suggested shuffles were not directly observed, most probably due to the high density of stacking faults in Type I twins.

The Type II boundary is found to be smooth and straight even at atomic scale and the estimated high index twin plane from stereographic projection agrees well with observations. The atomic configuration of Type II boundary is the simplest configuration, where only 1/12 of atoms need to shuffle within the interface about 0.262 Å. As expected, the twin boundary microstructure and shuffling process during twinning have a huge impact on the mobility of twin boundary, i.e. low twinning stress is related to the simplest, least shuffling required, stress-free and coherent boundary [46].

The high density of stacking faults at the Type I interface is always related to large strain field. This strain is caused by the binding of twinning dislocations at the interface. This can be the reason for high twinning stress of Type I twinning. In a bulk sample it is indeed quite difficult to experimentally activate the Type I twins which have twinning stress above 100 MPa [12]. However, in self-accommodated martensite we observed a relatively large amount of Type I twins containing high density stacking faults. We can speculate that the formation of Type I twinning and high density of stacking faults are due to a highly incompatible interface between austenite and martensite during phase transformation. These twins are wiped out during mechanical training, i.e. by repeating mechanical loading.

The question remains: how do these Type I twins disappear if their boundaries are not mobile compared to other twinning systems? From the morphology of Fig. 5, the particular coexistence of three types of twins suggests that the annihilation of Type I twinning is caused by joint moving of both Type II and compound twin boundaries. To be specific, and related to Fig. 5, the Type I pairs disappear due to the movement of the interface between A and B to the right. In other words, during deformation, the Type I twins are annihilated by the movement of twin boundaries of compound and Type II twins as they were favored by stress.

5. Conclusion

Morphology, crystallographic features and relationships of Type I, Type II, and compound twinning modes in 2H martensite of $Cu_{69.4}Ni_{3.4}Al_{27.2}$ shape memory alloy single crystal have been investigated in detail. In the self-accommodated case, the three twinning modes can coexist and are crystallographically related to each other. In the deformed state, Type I twins are annihilated and the compound twins are coupled with the remaining Type II twins even after mechanical training or repeated compression in two perpendicular directions.

The compound twin boundary is the most common and flexible. The boundary forms perfect coherent interplanar interface which results in low interface energy. The stretched-out interface is energetically favorable with the smallest shuffling needed at the interface. Such configuration results in the lowest twinning stress.

Type II twin boundary is also highly mobile which is due to a fully relaxed atomic configuration without strain field at the interface and to a small number of atoms which need a small shuffling. The experimentally determined plane of Type II twin boundaries agrees well with irrational twin planes predicted from the elastic continuum calculation.

Type I twinning boundary is the structurally most complex boundary, with half or all atoms at the interface shuffling to rather large distances. Furthermore, the atomic structure of the boundary is strongly affected by the high density of stacking faults. At stacking fault-free areas, the atomic configuration is highly stressed, as confirmed by HRTEM images.

To conclude, the twin shear, magnitude, and nature of shuffling of atoms at the interface and microstructure of the twin boundary are major factors affecting twin boundary mobility or twinning stress. We believe that this case can be a good approximation for twin boundaries in monoclinic martensite of ferromagnetic Ni-Mn-Ga alloy in which the extremely high mobility of twin boundaries is crucial for the existence of magnetic shape memory effect and can serve for theoretical approaches to describe and understand twin boundary in this ferromagnetic material.

Acknowledgements:

CzechNanoLab project LM2018110 funded by MEYS CR is gratefully acknowledged for the financial support of the measurements at LNSM Research Infrastructure. We would like to acknowledge financial support of the ERDF in the frame of the project SOLID21 (No. CZ.02.1.01/0.0/0.0/16_019/0000760) and M.K. to project No. CZ.02.1.01/0.0/0.0/15_003/0000485. The stay of Y. Ge in Prague was partially supported by CSF, grant No. 16-00062S. Further work of P.V. was supported by CSF, grant No. 21-06613S.

References

[1] K. Otsuka, C.M. Wayman, Shape Memory Materials, Cambridge University Press, 1999.

[2] Y. Song, X. Chen, V. Dabade, T.W. Shield, R.D. James, Enhanced reversibility and unusual microstructure of a phase-transforming material, Nature. 502 (2013) 85–88.

[3] C. Bechtold, C. Chluba, R. Lima de Miranda, E. Quandt, High cyclic stability of the elastocaloric effect in sputtered TiNiCu shape memory films, Appl. Phys. Lett. 101 (2012) 091903.

[4] V. Novák, P. Šittner, S. Ignacová, T. Černoch, Transformation behavior of prism shaped shape memory alloy single crystals, Mater. Sci. Eng. A. 438–440 (2006) 755–762.

[5] Z. S. Basinski, J.W. Christian, Crystallography of deformation by twin boundary movements in indium-thallium alloys, Acta Metall. 2 (1954) 101–116.

[6] J. Wang, H. Sehitoglu, Twinning stress in shape memory alloys: Theory and experiments, Acta Mater. 61(2013) 6790-6801.

[7] K. Ullakko, J.K. Huang, C. Kantner, R.C. O'Handley, V.V. Kokorin, Large magnetic-field-induced strains in Ni2MnGa single crystals, Appl. Phys. Lett. 69 (1996) 1966–1968.

[8] O. Heczko, N. Scheerbaum, O. Gutfleisch, Magnetic Shape Memory Phenomena, in: J.P. Liu, E. Fullerton, O. Gutfleisch, D.J. Sellmyer (Eds.), Nanoscale Magn. Mater. Appl., Springer US, 2009: pp. 399–439.

[9] A. Sozinov, N. Lanska, A. Soroka, W. Zou, 12% magnetic field-induced strain in Ni-Mn-Ga-based non-modulated martensite, Appl. Phys. Lett. 102 (2013) 021902–5..

[10] H.H. Liebermann, C.D. Graham, Plastic and magnetoplastic deformation of Dy single crystals, Acta Metall. 25 (1977) 715–720.

[11] Y. Ge, N. Zárubová, O. Heczko, S.-P. Hannula, Stress-induced transition from modulated 14M to non-modulated martensite in Ni–Mn–Ga alloy, Acta Mater. 90 (2015) 151–160.

[12] M. Vronka, H. Seiner, O. Heczko, Temperature dependence of twinning stress – Analogy between Cu–Ni–Al and Ni–Mn–Ga shape memory single crystals, Philos. Mag. 0 (2017) 1–19.

[13] V. Novák, P. Šittner, D. Vokoun, N. Zárubová, On the anisotropy of martensitic transformations in Cu-based alloys, Mater. Sci. Eng. A. 273–275 (1999) 280–285.

[14] T.W. Shield, Orientation dependence of the pseudoelastic behavior of single crystals of Cu□Al□Ni in tension, J. Mech. Phys. Solids. 43 (1995) 869–895.

[15] C. Rodriguez, L.C. Brown, Transitions between stress-induced martensites in Cu Al Ni alloys, Metall. Trans. A. 7 (1976) 265–272.

[16] O. Heczko, M. Vronka, P. Veřtát, M. Rameš, K. Onderková, V. Kopecký, P. Krátká, Y. Ge, Mechanical Stabilization of Martensite in Cu–Ni–Al Single Crystal and Unconventional Way to Detect It, Shape Mem. Superelasticity, 4 (2018) 77-84.

[17] A.M. Condó, F.C. Lovey, V. Torra, Interaction of twin boundaries with stacking faults in 2H martensite: A high-resolution electron microscopy study, Philos. Mag. 83 (2003) 1479–1493.

[18] A.G. Khachaturyan, S.M. Shapiro, S. Semenovskaya, Adaptive phase formation in martensitic transformation, Phys. Rev. B. 43 (1991) 10832–10843.

[19] S. Kaufmann, U.K. Rößler, O. Heczko, M. Wuttig, J. Buschbeck, L. Schultz, S. Fähler, Adaptive Modulations of Martensites, Phys. Rev. Lett. 104 (2010).

[20] M. Zelený, L. Straka, A. Sozinov, O. Heczko, Transformation Paths from Cubic to Low-Symmetry Structures in Heusler Ni 2 MnGa Compound, Sci. Rep. 8 (2018) 7275.

[21] K. Bhattacharya, Microstructure of Martensite: Why it forms and how it gives rise to the shape-memory effect, OUP Oxford, 2003.

[22] U. Sarı, İ. Aksoy, Electron microscopy study of 2H and 18R martensites in Cu–11.92wt% Al–3.78wt% Ni shape memory alloy, J. Alloys Compd. 417 (2006) 138–142.

[23] T. Hara, T. Ohba, S. Miyazaki, K. Otsuka, Electron Microscopy Study of Type II Twins in γ1′ Cu－Al－Ni Martensite, Mater. Trans. JIM. 33 (1992) 1105-1113.

[24] J.W. Christian, S. Mahajan, Deformation twinning, Prog. Mater. Sci. 39 (1995) 1–157.

[25] M. Han, J.C. Bennett, M.A. Gharghouri, J. Chen, C.V. Hyatt, N. Mailman, Microstructure characterization of the non-modulated martensite in Ni–Mn–Ga alloy, Mater. Charact. 59 (2008) 764–768.

[26] K. Otsuka, K. Shimizu, Twinning in γ′ Cu – Al – Ni Martensite with Cu3Ti Type Ordered Structure, Trans. Jpn. Inst. Met. 15 (1974) 109-113.
[27] K. Otsuka, K. Shimizu, Morphology and Crystallography of Thermoelastic γ' Cu-Al-Ni Martensite, Jpn. J. Appl. Phys. 8 (1969) 1196.
[28] M. Vronka, M. Karlik, J. Vesely, J. Manak, O. Heczko, Suppression of twinning mechanism on nanoscale: size effect in Cu–Ni–Al shape memory alloy, J. Mater. Sci. 54 (2019) 6586–6593.
[29] D. Liu, H. Hashimoto, T. Ko, Electron microscopy study of martensite in Cu–11.2 wt% Al–3 wt% Ni, J. Mater. Sci. 32 (1997) 1657–1663.
[30] S. Ichinose, Y. Funatsu, K. Otsuka, Type II deformation twinning in γ′ 1 martensite in a Cu-Al-Ni alloy, Acta Metall. 33 (1985) 1613 – 1620.
[31] A. Saren, A. Sozinov, S. Kustov, K. Ullakko, Stress-induced a/b compound twins redistribution in 10M Ni-Mn-Ga martensite, Scr. Mater. 175 (2020) 11–15.
[32] L. Straka, N. Lanska, K. Ullakko, A. Sozinov, Twin microstructure dependent mechanical response in Ni–Mn–Ga single crystals, Appl. Phys. Lett. 96 (2010) 131903.
[33] O. Heczko, P. Veřtát, M. Vronka, V. Kopecky, O. Perevertov, Ni–Mn–Ga Single Crystal Exhibiting Multiple Magnetic Shape Memory Effects, Shape Mem. Superelasticity. 2 (2016) 272–280.
[34] N. Zárubová, Y. Ge, O. Heczko, S.-P. Hannula, In situ TEM study of deformation twinning in Ni-Mn-Ga non-modulated martensite, Acta Mater. 61 (2013) 5290–5299.
[35] K. Momma, F. Izumi, VESTA 3 for three-dimensional visualization of crystal, volumetric and morphology data, J. Appl. Crystallogr. 44 (2011) 1272–1276.
[36] M. Vronka, L. Straka, H. Seiner, M. Karlík, O. Heczko, Mechanical Stabilization of Martensite: Comparison of Ni-Mn-Ga and Cu-Ni-Al Shape Memory Single Crystals, Acta Phys. Pol. A. 134 (2018) 627–630.
[37] Y. Ge, H. Jiang, A. Sozinov, O. Soederberg, N. Lanska, J. Keraenen, E.I. Kauppinen, V.K. Lindroos, S.P. Hannula, Crystal structure and macrotwin interface of five-layered martensite in Ni-Mn-Ga magnetic shape memory alloy, Mater. Sci. Eng. Struct. Mater. Prop. Microstruct. Process. 438–440 (2006) 961–964.
[38] M. Han, F.F. Kong, Twin boundary structure of the modulated variants in a Ni–Mn–Ga alloy, J. Alloys Compd. 458 (2008) 218–222.
[39] M. Han, J.C. Bennett, M.A. Gharghouri, J. Chen, C.V. Hyatt, Understanding modulated twin transition at the atomic level, Acta Mater. 55 (2007) 1731–1740.
[40] A.M. Condó, F.C. Lovey, V. Torra, Interaction of twin boundaries with stacking faults in 2H martensite: A high-resolution electron microscopy study, Philos. Mag. 83 (2003) 1479–1493.
[41] A.S.K. Mohammed, H. Sehitoglu, Strain-sensitive topological evolution of twin interfaces, Acta Mater. 208 (2021) 116716.
[42] R. Chulist, K. Nalepka, A. Sozinov, Hierarchical twin microstructure in modulated 10M Ni–Mn-Ga single crystals. An analysis including shuffling of atomic layers, Int. J. Plast. 126 (2020) 102628.
[43] D. Shilo, E. Faran, B. Karki, P. Müllner, Twin boundary structure and mobility, Acta Materialia. 220 (2021) 117316.
[44] M. Matsuda, Y. Yasumoto, K. Hashimoto, T. Hara, M. Nishida, Transmission Electron Microscopy of Twins in 10M Martensite in Ni–Mn–Ga Ferromagnetic Shape Memory Alloy, Mater. Trans. 53 (2012) 902–906.
[45] B. Karki, P. Müllner, R. Pond, Topological model of type II deformation twinning in 10M Ni-Mn-Ga, Acta Materialia. 201 (2020) 604–616.
[46] T. Ezaz, H. Sehitoglu, Type II detwinning in NiTi, Appl. Phys. Lett. 98 (2011) 141906.

Figure 1

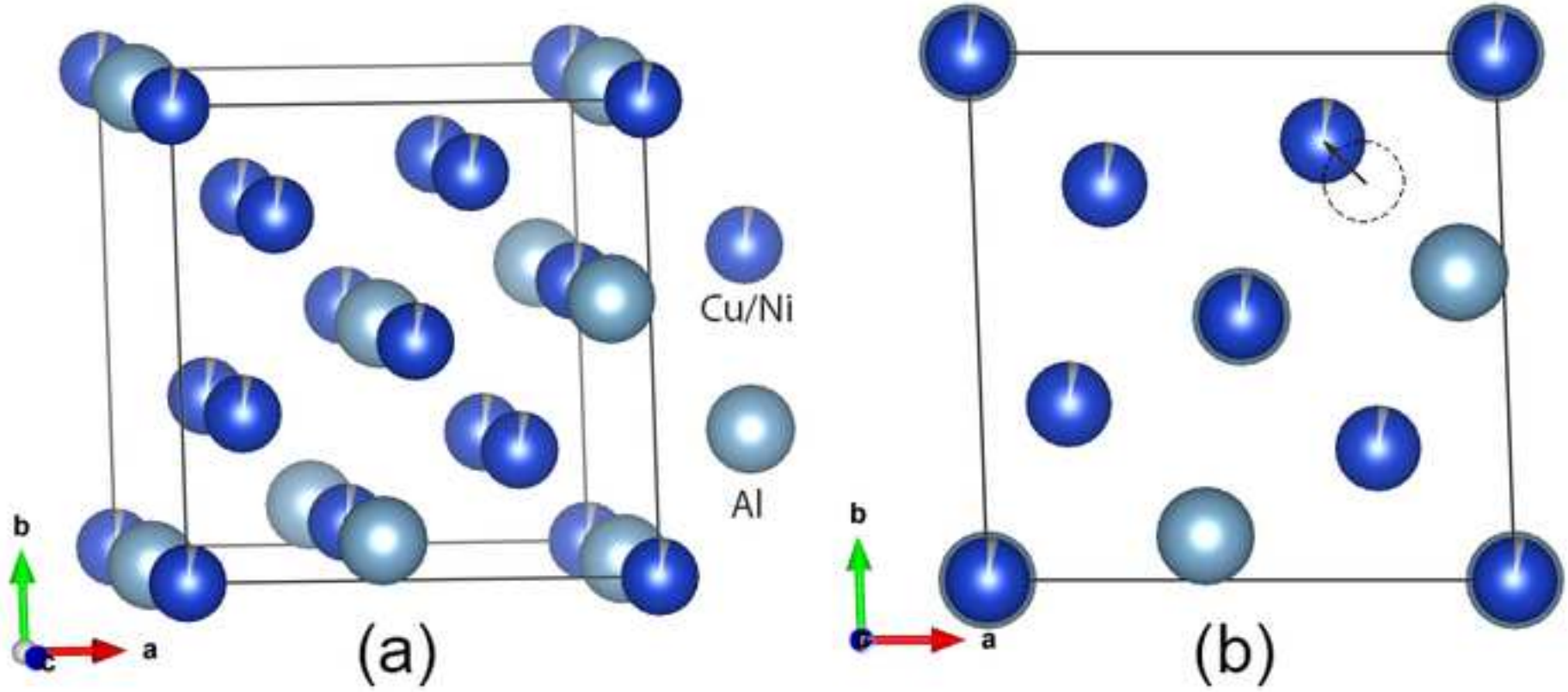

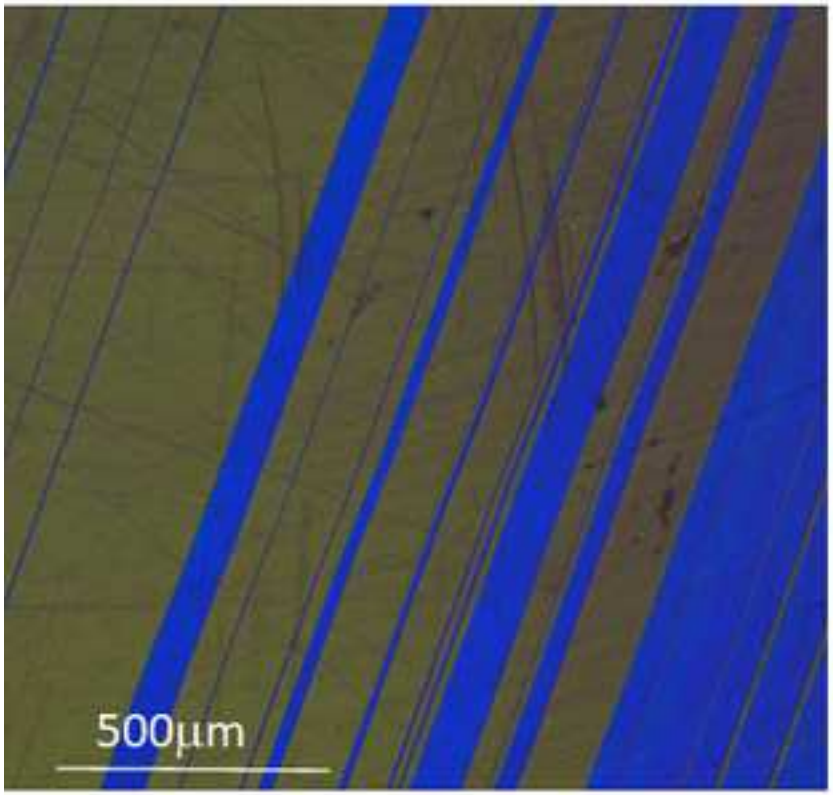

(a)

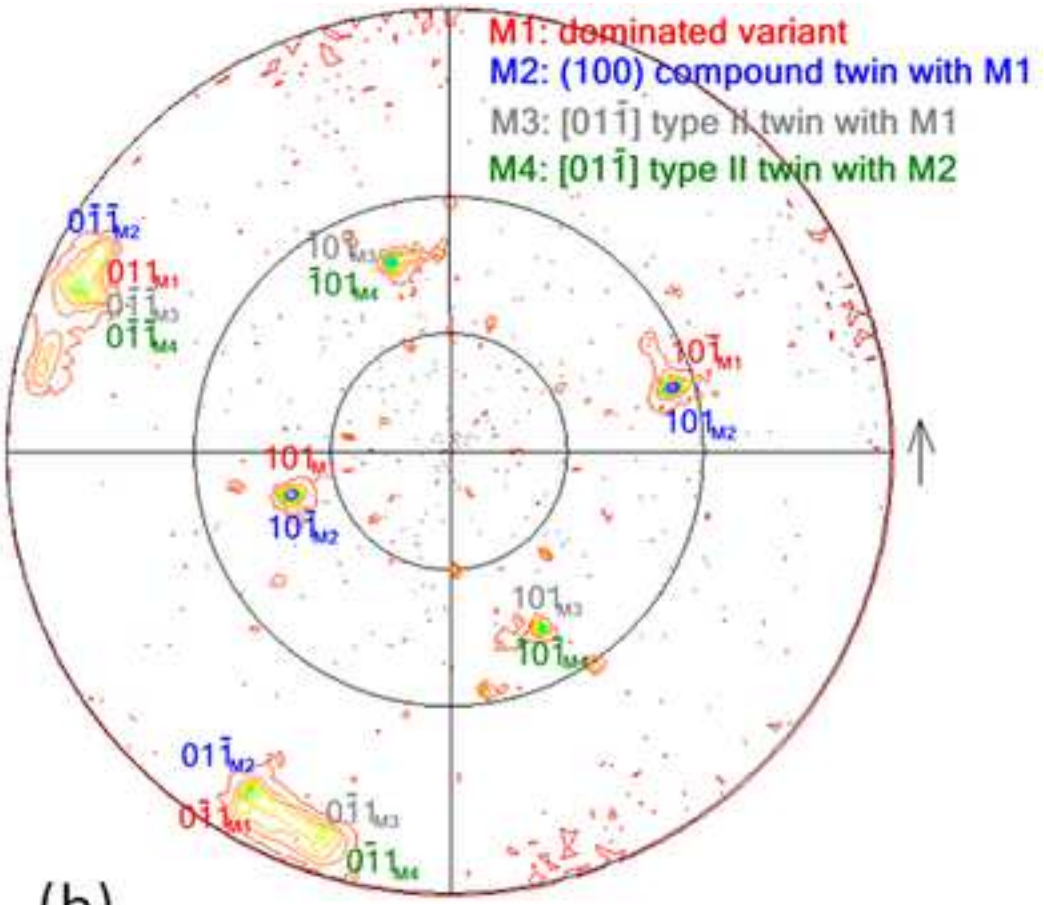

(b)

Figure 3

Click here to access/download;Figure(s);Fig3.tif

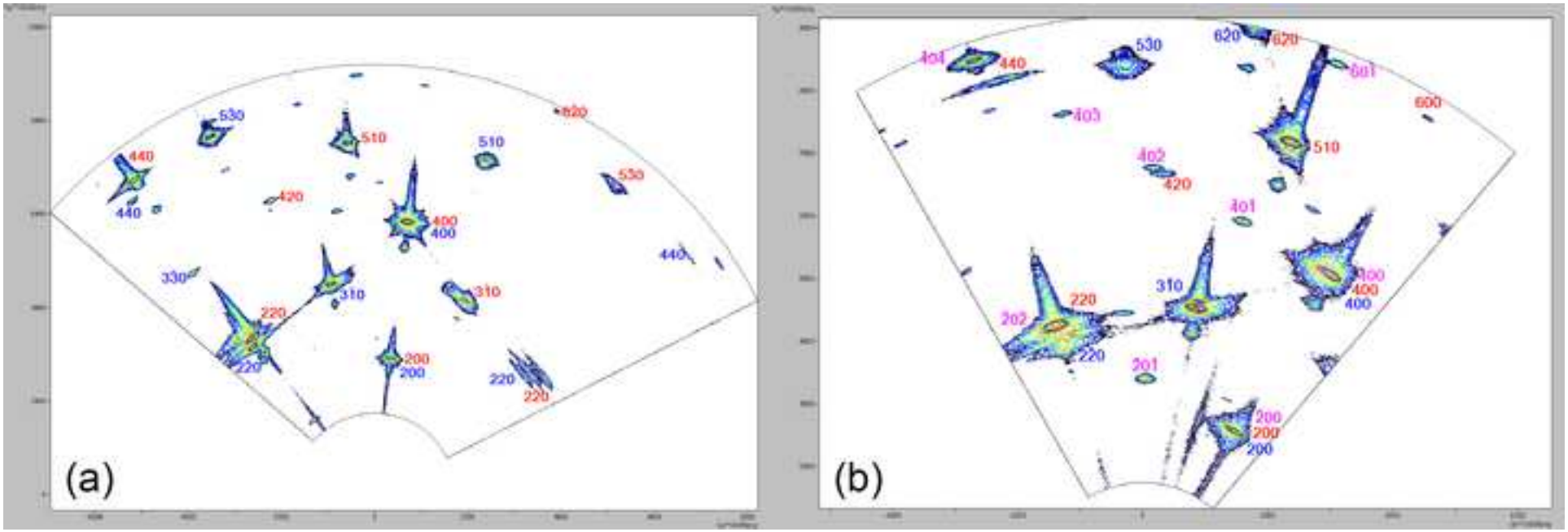

Figure 4

Click here to access/download;Figure(s);Fig4.tif

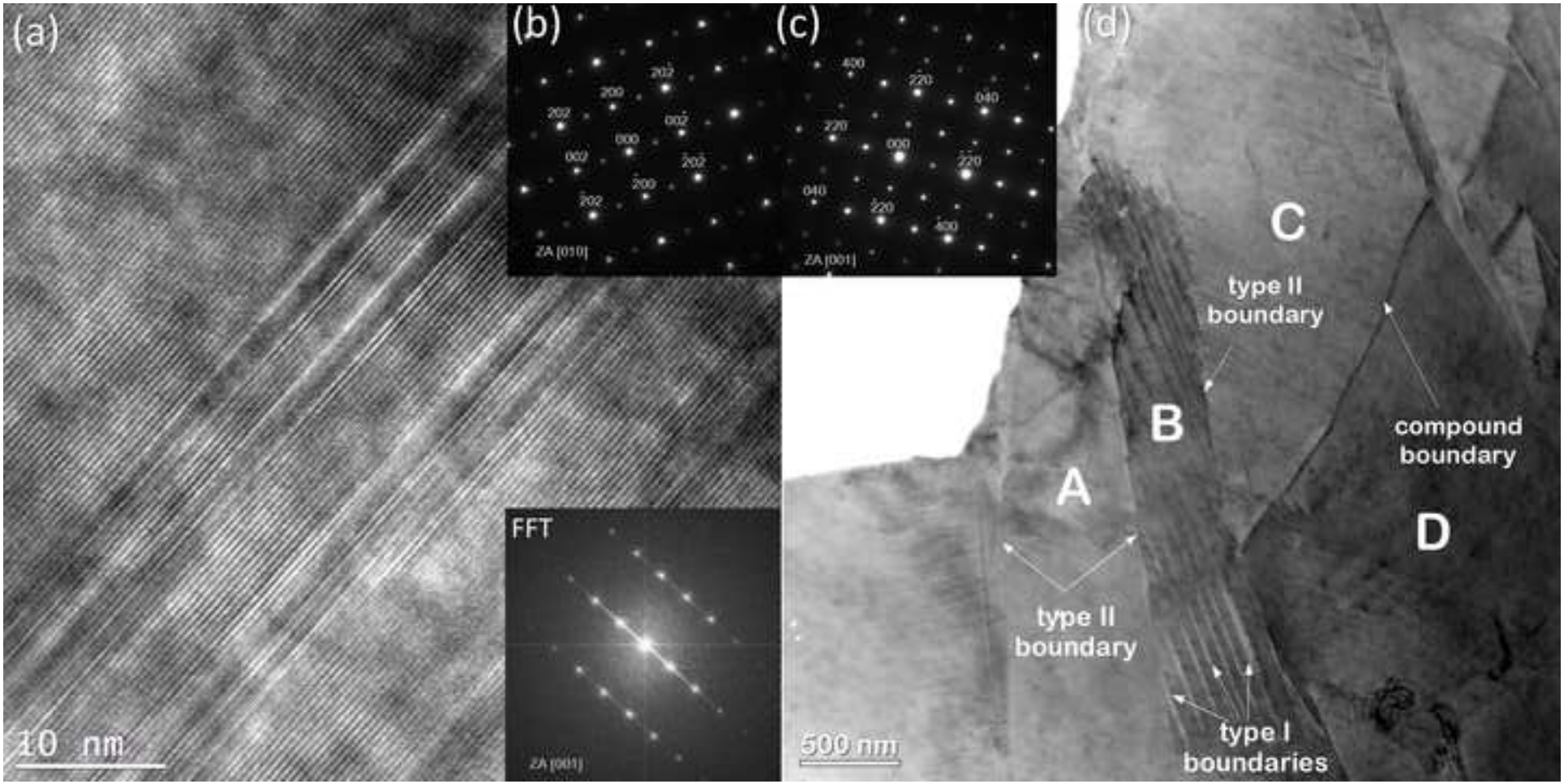

Figure 5

Click here to access/download;Figure(s);fig5.tif

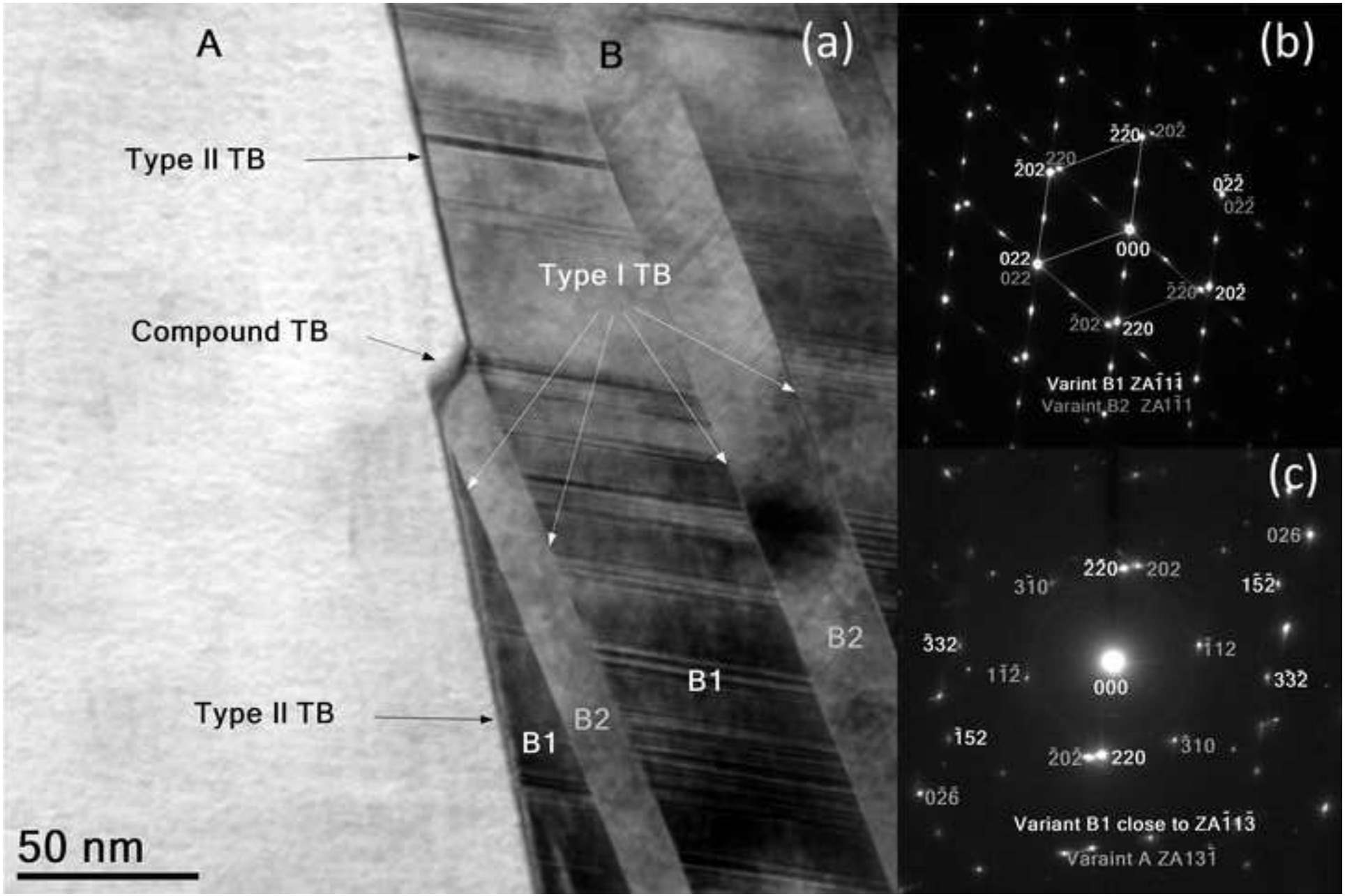

Figure 6

Click here to access/download;Figure(s);fig6.tif

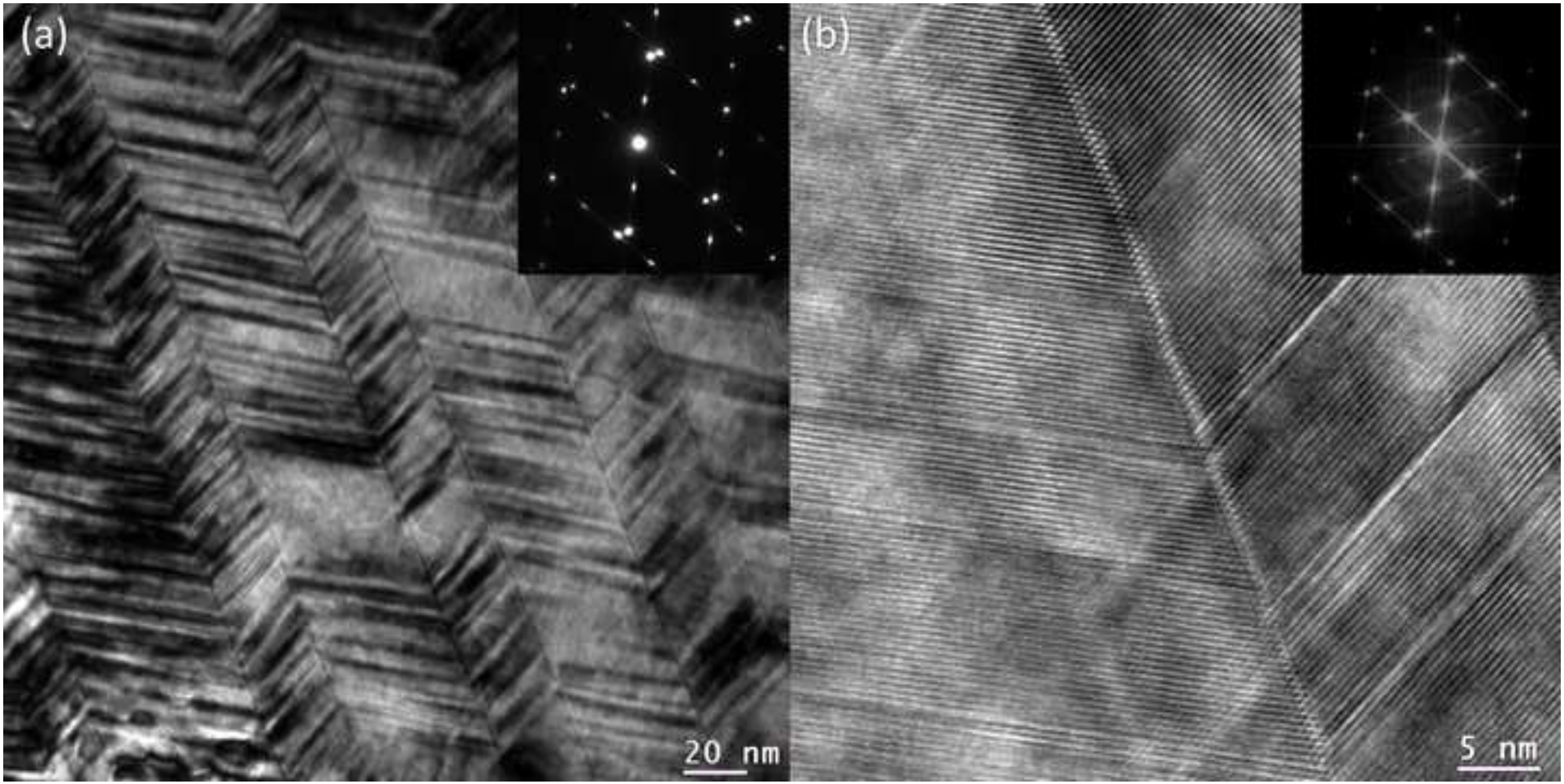

Figure 7

Click here to access/download;Figure(s);fig7.tif

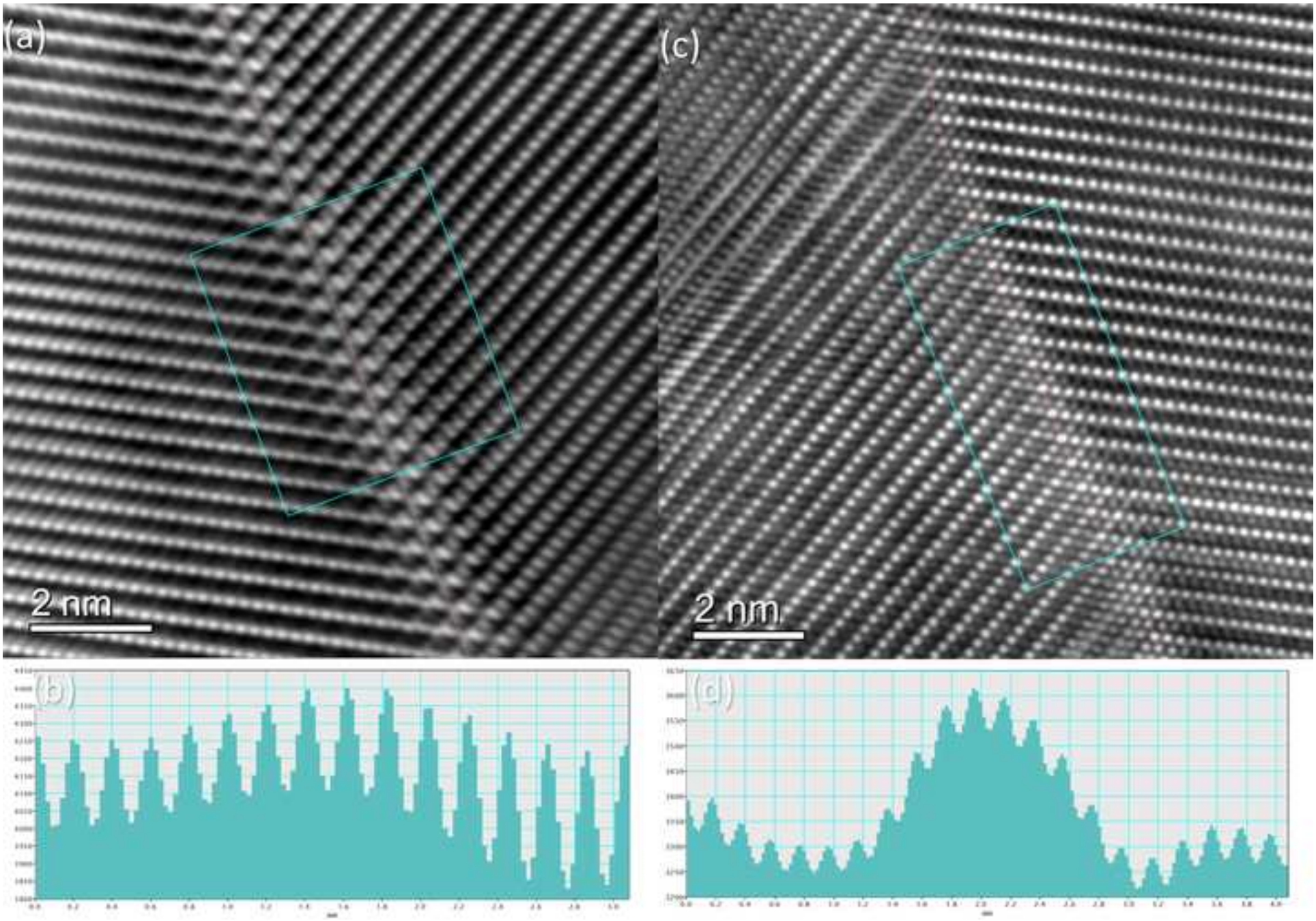

Figure 8

Click here to access/download;Figure(s);fig8.tif

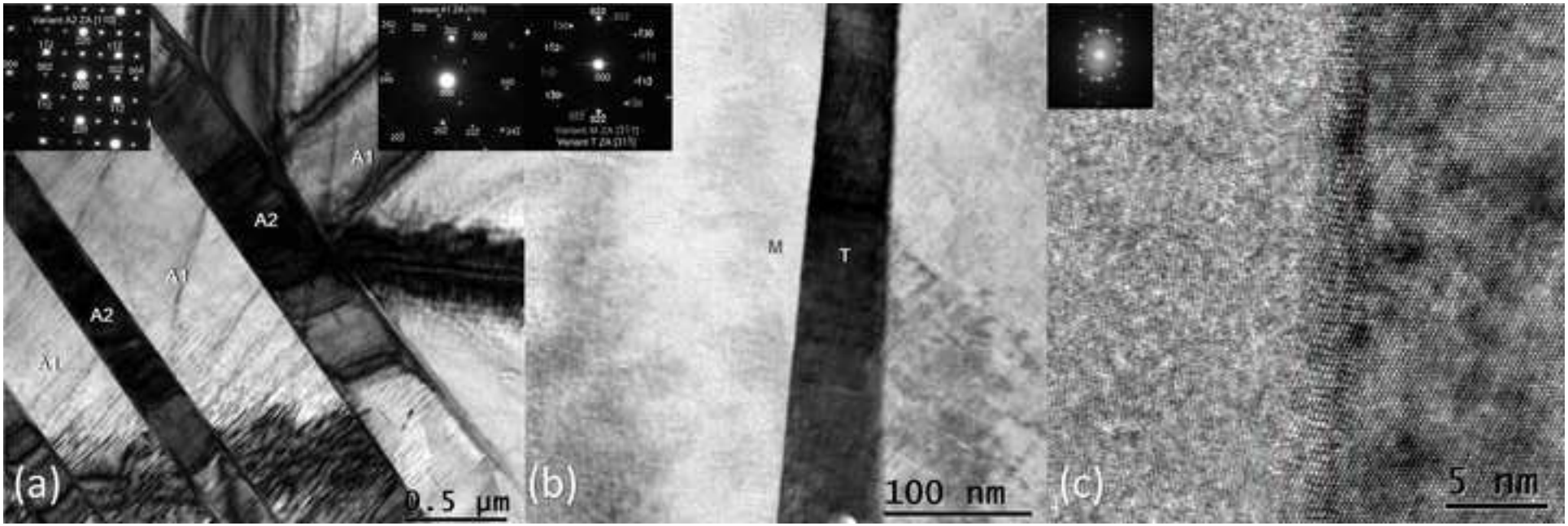

Figure 9

Click here to access/download;Figure(s);fig9.tif

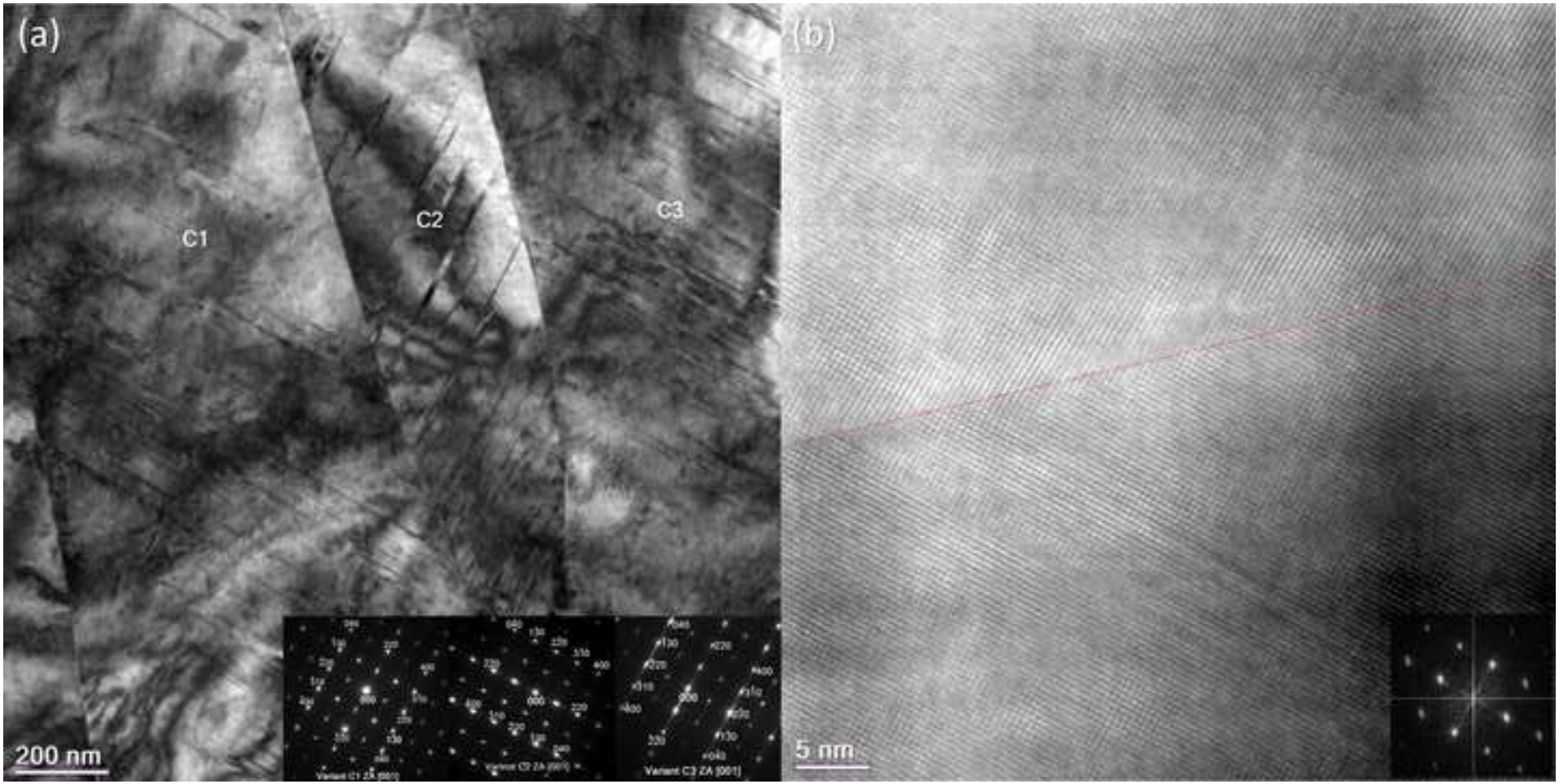

Figure 10

Click here to access/download;Figure(s);fig10.tif

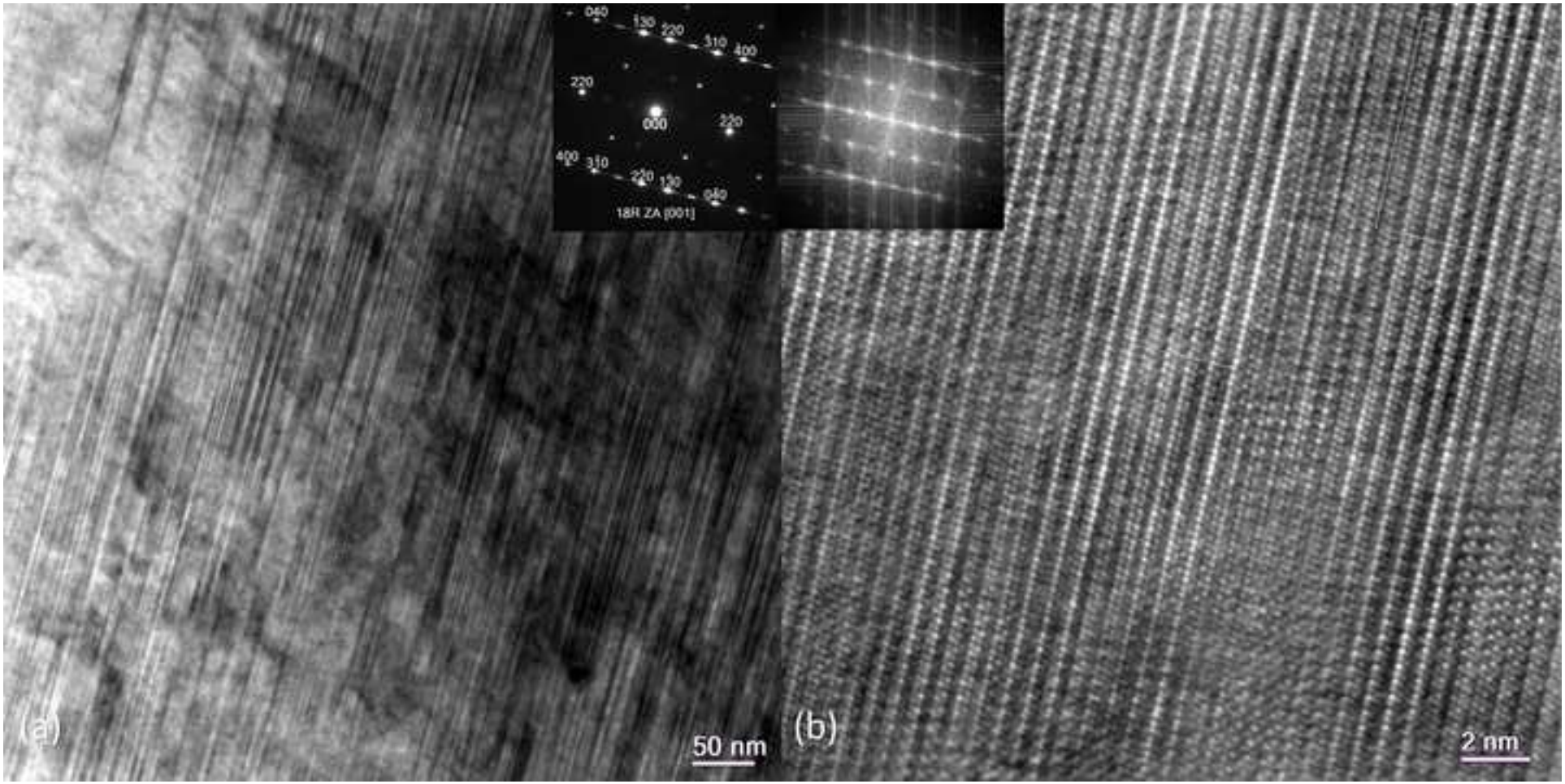

Figure 12

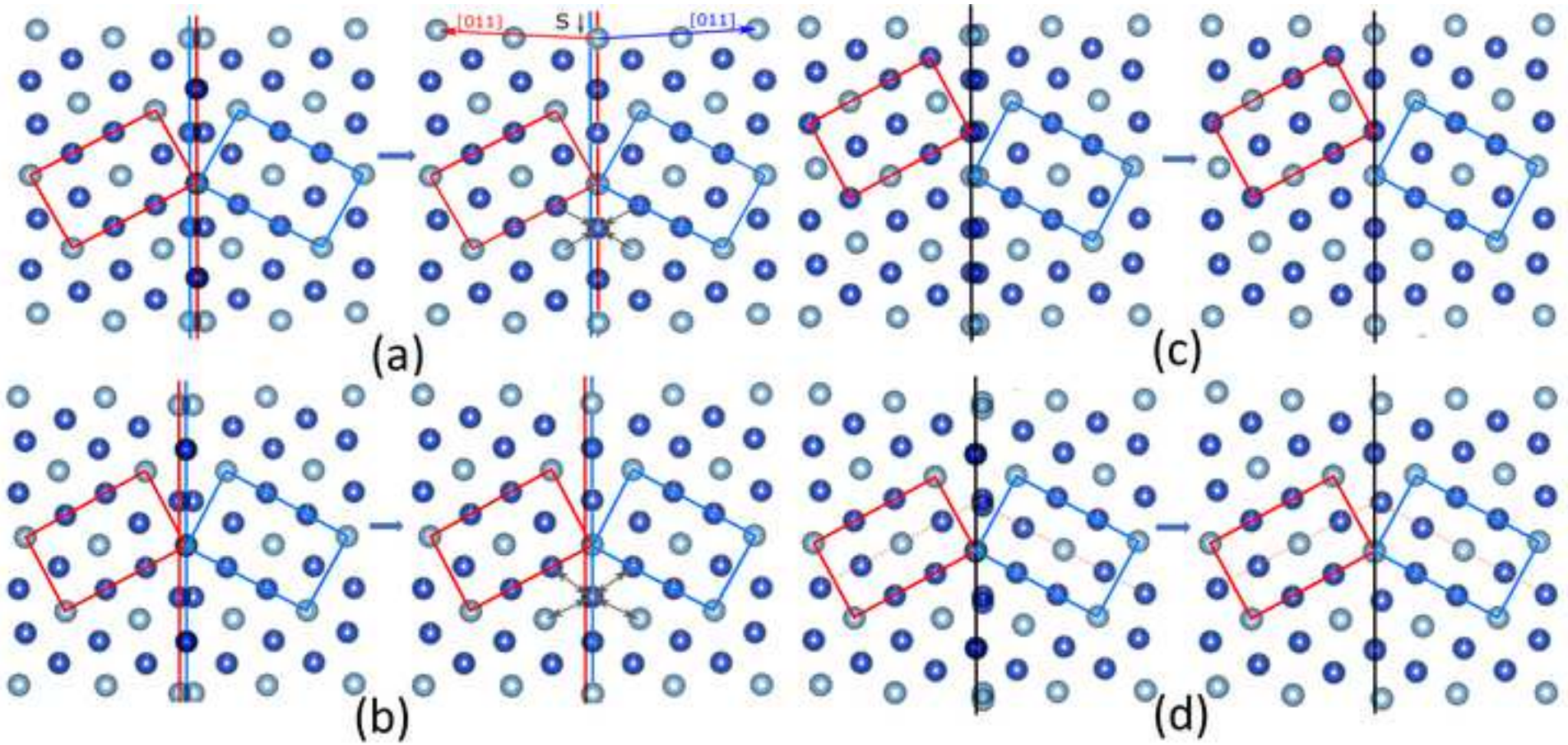

Figure 13

Click here to access/download;Figure(s);Fig13.tif

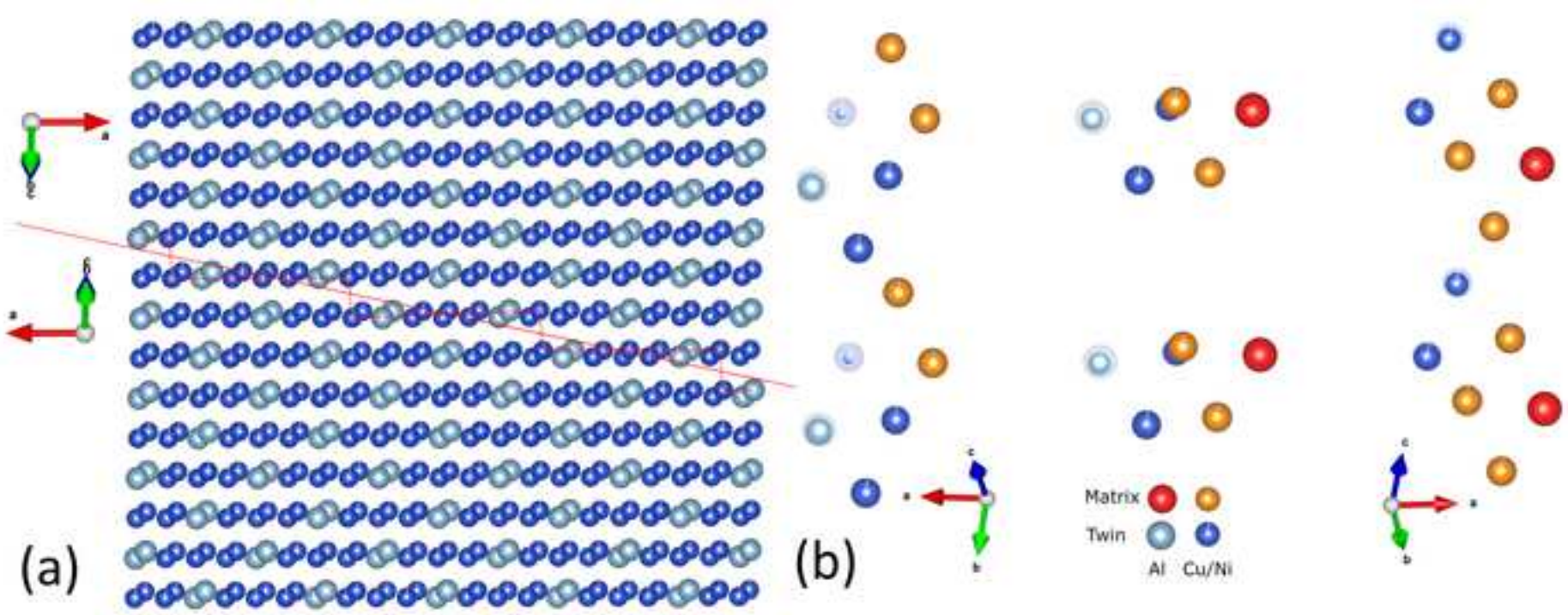

Figure 14

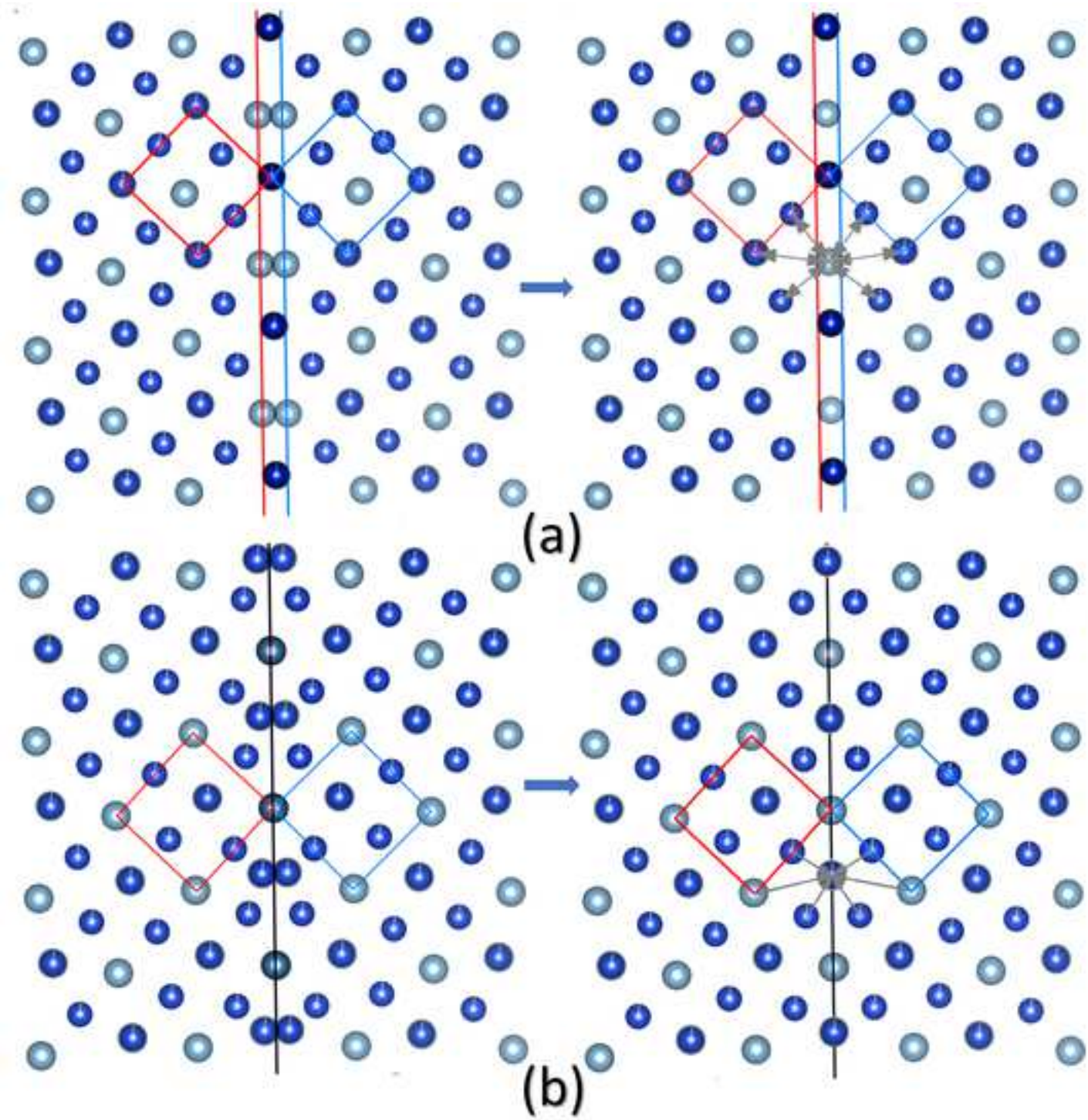

Graphical Abstract

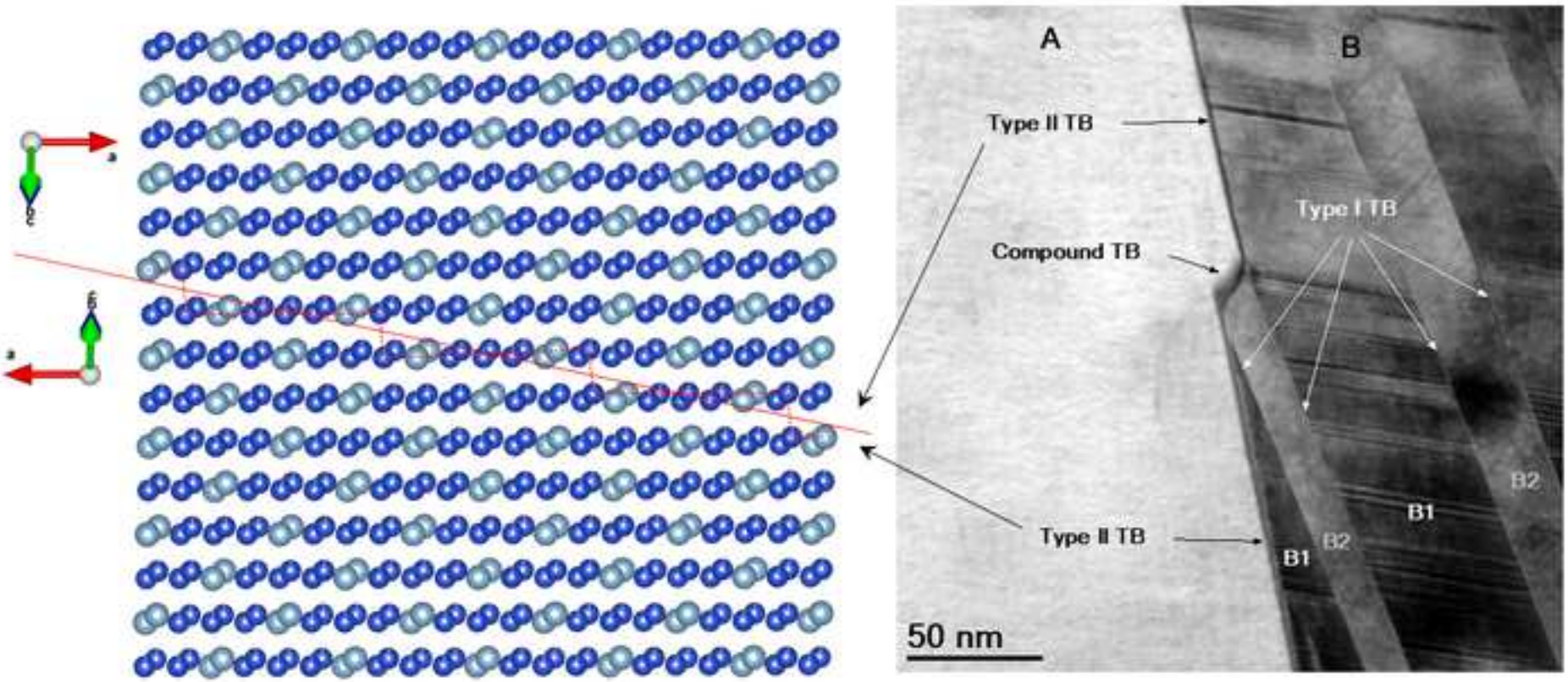

Declaration of interests

☒ The authors declare that they have no known competing financial interests or personal relationships that could have appeared to influence the work reported in this paper.

☐The authors declare the following financial interests/personal relationships which may be considered as potential competing interests:
